Scalable and sustainable manufacturing of ultrathin metal–organic framework nanosheets (MONs) for solar cell applications

David J. Ashworth [a,1], Justin Driver [a,b], Kezia Sasitharan [a,2], Ram R.R. Prasad [a], Joshua Nicks [a,3], Benedict J. Smith [a], Siddharth V. Patwardhan [b], Jonathan A. Foster [a,*]

[a] Department of Chemistry, The University of Sheffield, Brook Hill, Sheffield S3 7HF, UK
[b] Department of Chemical and Biological Engineering, The University of Sheffield, Mappin Street, Sheffield S1 3JD, UK

ARTICLE INFO

ABSTRACT

Metal-organic framework nanosheets (MONs) are an emerging class of 2D materials whose tunable chemistry make them ideal for a wide range of sensing, catalytic, electronics and separation applications. However, creating scalable routes to the synthesis of high quality, ultrathin nanosheets remains challenging and little consideration has been given to the economics of making these materials. Here, we demonstrate a scalable synthesis of zinc-porphyrin based nanosheets, $Zn_2(H_2TCPP)$, for use in organic solar cells and conduct a techno-economic analysis of their pilot-plant scale manufacture. A thorough investigation of the process chemistry of the solvothermal synthesis enabled reduction of reaction time, increased solid content and scale-up of the reaction in batch. Significantly, the addition of triethylamine accelerated the reaction kinetics, which enabled the synthesis temperature to be dropped from $> 80\ °C$ to room temperature. Application of these new reaction conditions in a continuous stirred-tank reactor directly formed monolayer MONs at 99 % yield with a space–time yield of 16 kg m^{-3} day^{-1}, an approximately 20-fold increase in yield compared to adapting the literature procedure. Techno-economic analysis showed a 94 % reduction in the production costs compared to the literature reaction conditions and indicated that the production cost was dominated by ligand price. The general applicability of the method was demonstrated through synthesis of related $Cu_2(H_2TCPP)$ MONs and tunability through metalation of the porphyrin units with six different metal ions. Finally, the value of the nanosheets was demonstrated through a near doubling in the power conversion efficiency of organic photovoltaic devices when the MONs were incorporated into the active layer. Overall, this work demonstrates the first scalable and sustainable route to producing monolayer nanosheets for high value applications.

1. Introduction

Metal-organic framework nanosheets (MONs) are a promising new class of nanomaterial which combine the high surface area and nanoscopic dimensions of two-dimensional (2D) materials with the modular structures and diverse chemistry of metal–organic frameworks (MOFs) [1]. MONs have already shown exceptional early performance across a wide range of sensing, catalysis, electronics and separation applications [2–5]. A diverse range of lab-scale approaches to the synthesis of different MONs have been investigated [6–9]. These can be divided into

"top-down" approaches, in which a layered metal–organic framework (MOF) is exfoliated through liquid-assisted ultrasonication [10], shear-mixing [11], and grinding/ball-milling [12] as well as "bottom up" approaches where nanosheets are assembled directly, usually with the aid of interfaces, [13–15] surfactants [16–18] or templates [19,20] to promote two-dimensional growth. However, in most cases only minute (mg) quantities of nanosheets are produced as dilute suspensions through low yielding processes conducted at high temperatures with long reaction times. New scalable routes are therefore required to enable economic production of promising MONs for use in applied settings

[21].

Continuous production processes offer significant advantages over batch reactions in large scale production, such as reduced down times, labour costs and reactor volumes as well as more consistent products and higher space time yields (STY) [22,23]. A variety of continuous production methods have been developed to scale-up the manufacture of three-dimensional metal–organic frameworks (MOFs) including thermal, electrochemical and mechanochemical processes, [24–27] and MOFs are being commercialised by BASF, and others.

The need to prevent particle aggregation and intergrowth for anisotropic MONs poses additional challenges for the synthesis of MONs. To our knowledge, only two examples have so far been reported of MONs synthesised through continuous processes [28]. In 2018, Thomas and co-workers applied a microdroplet flow reaction set-up to synthesise ∼ 250 mg of multilayer (down to ∼ 3 nm, three layers thick) Zr (BTB) (BTB = 1,3,5-tris(4-carboxyphenyl)benzoate) MONs of lateral dimensions up to 3 μm, with a space–time yield (STY) of ∼ 385 kg m^{-3} day^{-1} [29]. In 2020, Lapkin and co-workers demonstrated the synthesis of ∼ 250 mg of Cu(BDC) MONs with a much higher STY of ∼569,000 kg m^{-3} day^{-1}, with tightly controlled lateral dimensions < 50 nm and thicknesses down to monolayer, using a high shear annular microreactor [30]. The high capital and operational expenditure associated with scaling-out microfluidics and the specialist equipment required with high shear annular microreactors limit their potential beyond high value, low volume manufacture of speciality products. New synthetic routes which facilitate the scale-up of MON manufacture using well-established, operationally easy equipment are required to make MONs attractive for industrial applications.

Continuous stirred-tank reactors (CSTRs) are widely used in the pharmaceutical and fine chemicals industry and provide an attractive alternative approach for achieving scalable MON production [31,32]. We have previously developed the first CSTR synthesis for MOF-5 [33] and mapped the synthesis process parameters [34]. CSTRs offers consistent particle production after the reactor has reached a steady state, which eliminates the potential variability often observed between identical batch syntheses of MOFs [35]. Importantly, the shape of CSTR reactors are such that reaction conditions remain constant regardless of the size of the vessel, provided mixing and heating remain efficient. The kinetics in CSTR reactors are different from those in previous examples of continuous synthesis as reagents are immediately diluted to their minimum concentration and this is maintained throughout the reaction. We hypothesised the CSTR set-up could therefore bring benefits in controlling the kinetics of nanosheet growth and maintaining stable dispersions to enable the scalable production of monolayer nanosheets.

MONs based on tetra(carboxy)porphyrin ligands are amongst the earliest and most widely investigated [36]. The planar structures and high connectivities make them ideal candidates for the formation of high aspect ratio nanosheets, with useful optoelectronic properties and accessible metal sites. This distinct combination of properties has lead them to be used in therapeutic treatments, [37,38] electro- and photo-catalysis, [39] biological sensing, [40–43] energy storage, [44] separation [45–47] and electronics [48] applications. We recently showed how the addition of Zn$_2$(ZnTCPP) (where H$_6$TCPP = tetrakis(4-carboxyphenyl)porphyrin) nanosheets to organic solar cells lead to a near doubling in their power conversion efficiency [49] and allowed us to produce the highest performing fullerene-based organic photovoltaic (OPV) devices in the literature [50].

Keen to capitalise on these exciting results, we sought to find a scalable route to the synthesis of these nanosheets. Zn$_2$(ZnTCPP) was first synthesised as a MOF by Choi *et al* in 2009 *via* a solvothermal synthesis (3:1 DMF:EtOH, 80 °C, 24 h) [51]. This was adapted in 2015 by Zhang and co-workers who showed that PVP (polyvinylpyrrolidone) could be used as a crystal growth modifier, providing a bottom-up synthesis for nanosheets of [Zn$_2$(ZnTCPP)] [52,53]. Anticipating the PVP would interfere with device performance or require extensive washing procedures to remove, we created monolayer nanosheets of

Zn$_2$(ZnTCPP) *via* a top down approach using ultrasonic liquid exfoliation [49,50]. However, in all cases, batch processes, long reaction times, high temperatures, dilute concentrations and additional steps are required to form and/or isolate nanosheets and therefore do not lend themselves to scale-up.

Here, we 1) explore the process chemistry to design and use industrially relevant CSTRs to demonstrate the first scalable route to the synthesis of porphyrin MONs, 2) investigate the factors affecting the economics of manufacture, and 3) demonstrate a high value application for the materials produced. A previously reported batch synthesis for Zn$_2$(ZnTCPP) MOF was systematically studied in order to reduce the reaction time, temperature and DMF content whilst maximising solid content and yield. Optimised conditions were used in a CSTR set-up to demonstrate the production of monolayer MONs with a high yield. A techno-economic analysis of the continuous production of MONs in pilot-plant scale was conducted for the first time, to investigate the impact of these changes on the cost of production and identify where future efforts should be focussed. The generality of the approach was then demonstrated through the synthesis of a copper-based analogue, and MON tunability shown through post-synthetic metalation of the MONs. Finally, the as-synthesised nanosheets were used as additives within the active layer of an OPV resulting in a near doubling of the power conversion efficiency of the devices.

2. Results and discussion

Synthetic methodologies for Zn$_2$(ZnTCPP) MOF typically use adaptations of that first reported by Choi *et al.* in 2009 [51]. Solvothermal syntheses are performed in 3:1 vol:vol mixtures of DMF:EtOH (DMF = *n*, *n*-dimethylformamide, EtOH = ethanol) or DEF:EtOH (DEF = *n,n*-diethylformamide) for 16–24 h at 80 °C, with yields of the layered MOF ranging 53–87 %. Zhang and co-workers demonstrated a bottom-up route of MON synthesis in 2015 using conditions inspired by the initial MOF synthesis, but at lower concentration and adding PVP into the reaction mixture prior to solvothermal treatment [52]. The reagent concentrations corresponded to [solids] = 0.0625 wt%, and a total solvent volume of 16 mL was used. Other authors have used reaction times ranging from 16 to 24 h [47,52,53]. In our previous work, we adapted the synthesis used by Choi *et al.* to first make the layered MOF Zn$_2$(ZnTCPP) over 18 h at 80 °C without PVP (Fig. 1a) and then used ultrasonic liquid exfoliation (1 h) followed by centrifugation (10 mins) to isolate predominantly monolayer nanosheets (Fig. 1b) [49,50]. However, the prolonged reaction times used in all of these syntheses are not conducive to scalable MON manufacture, so we undertook a systematic study to optimise the reaction conditions for use in a CSTR set-up.

2.1. High-temperature syntheses

Initial studies were undertaken to investigate if the reaction time could be reduced, the concentration of reactants could be increased and the reaction scaled, starting from conditions used by Zhang *et al* [52]. See Section 4.2. and ESI Figs S1–S4 for details and characterisation of in-house synthesised H$_6$TCPP used in studies. To make the conditions more relevant to later studies, a stirrer bar was added to the reaction mixture, which was stirred throughout. Kinetic studies were performed at 80, 100 and 120 °C with six replicates which were stopped after 1, 2, 3, 4, 5, and 16 h by cooling the reaction vessel rapidly using iced water. Solids were immediately washed with EtOH through centrifugation and air-dried at room temperature. The mass of isolated dry solids was used to calculate the yield at each time point (Fig. 1c). After 5 h at the reference temperature of 80 °C, the yield was only 18 %, which increased to 60 % after 16 h. Increasing the temperature to 100 °C produced>80 % yields after 5 h. At 120 °C, just 1 h of reaction time yielded 87 %, increasing to 96 % after 3 h. PXRD indicated the same phase was produced in all cases (ESI Fig. S5) which matched that of Zn$_2$(ZnTCPP) [49]. It is likely that further
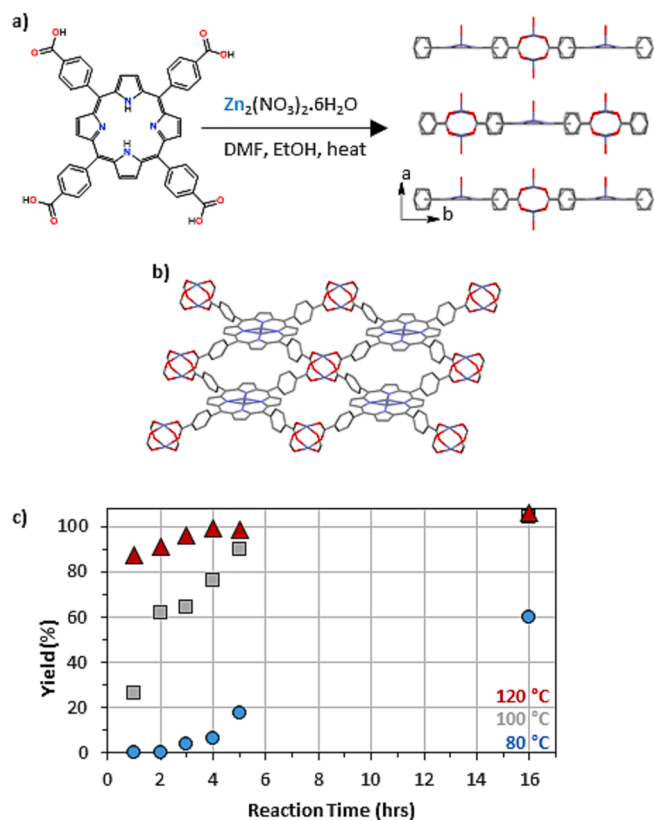
Fig. 1. Synthesis of Zn$_2$(ZnTCPP). a) Schematic of the synthesis of Zn$_2$(ZnTCPP) MOF, with crystal structure (CCDC 652596), and b) image of a single 2D layer. Hydrogens are omitted in both cases for clarity, and axially coordinated H$_2$O are not shown in b). Atomic colours are light blue, red, blue and grey for zinc, oxygen, nitrogen and carbon, respectively. c) Yield plot of kinetic studies of Zn$_2$(ZnTCPP) MOF synthesis at 80, 100 and 120 °C.

increase in the reaction temperature would result in even more rapid product formation, however these high temperatures are highly undesirable from both an energy cost, risk and environmental perspective.

Next, the reagent concentration was increased from 0.0625 wt% to 0.25, 0.5, 0.75 and 1 wt% and the reactions run with consistent reaction conditions of 120 °C for 1 h. [Solids] of 1 wt% required gentle heating to fully dissolve the H$_6$TCPP precursor. Purple solids were obtained with broadly consistent yields of 84, 71, 86 and 87 %, respectively (Table 1), and PXRD confirmed the expected phase in each case (ESI Fig. S6). These results indicate that the reaction concentration can be successfully scaled to 1 wt% with no detrimental effect to the yield or phase purity of Zn$_2$(ZnTCPP). It is possible that higher concentrations of solids could be used, but for continuous synthesis the limited solubility of the H$_6$TCPP at room temperature in the solvent mixture is likely to cause problems during scale-up.

To investigate the scalability of this methodology, the batch reaction was scaled up to a reactor volume of 200 mL (12.5-fold increase) which

Table 1
Yields of Zn$_2$(ZnTCPP) obtained under process intensification through batch syntheses.

[Solids] (wt %)	Vol. (mL)	Time (h)	Temp. (°C)	Yield (%)
0.0625	16	1	120	87
0.25	16	1	120	84
0.5	16	1	120	71
0.75	16	1	120	86
1	16	1	120	87
1	200	3	120	86

corresponded to 1 g of solids. The reaction was run using 1 wt% of solids at 120 °C for 3 h after which 858 mg of dried solids were isolated, corresponding to a 86 % yield. PXRD analysis was consistent with small batch syntheses (ESI Fig. S7) and previous literature for the Zn$_2$(ZnTCPP) phase. SEM of the dried solids (ESI Fig. S8) showed stacked lamellar square platelet morphologies with lateral dimensions <10 μm and thicknesses of <5 μm. Material produced this way would therefore require additional exfoliation steps in order to produce nanosheets, in line with our previous work.

We applied the knowledge gained through our exploration of the reaction space to a CSTR set-up (Fig. 2a). The reactor was initially set-up (see section 4.2.3.) to run using 0.0625 wt% solids with a temperature of 120 °C and a flow rate such that the average residence time was 50 min, which was expected to provide good yields based on the initial batch syntheses investigations. Given the high temperature of the reactor, the outlet flow was passed through a heat exchanger to cool to <25 °C before passing through the final peristaltic pump to protect the mechanics. Upon operation, the temperature inside the reactor was measured to be 113 °C, due to the boiling point depression caused by dissolved reagent in the reaction solution. Samples were collected at intervals of 14 mins (except the final sample, where collection was 7 min) for a total of 175 mins and solids washed through centrifugation with EtOH.

There was an initial lag-time observed in the formation of Zn$_2$(ZnTCPP) (Fig. 2b). Solids were first observed in the third fraction collected (28–42 min, 6 % yield), which increased up to a steady-state yield of ~ 28 % after approximately 1 h of operation and decreased again slightly after 150 mins to ~ 25 %. PXRD analyses of dried samples indicated that Zn$_2$(ZnTCPP) was formed phase-pure from the first observed solids (Figs. 2c, ESI S9). Some variations in peak intensity were observed between the different samples which was attributed to crystallite preferred orientation, due to highly anisotropic crystal growth. In contrast to previous work on MOF-5,[34] no intermediary solid phases were observed prior to formation of the desired MOF, which is consistent with other studies on MOFs such as UiO-66-NH$_2$[54] and HKUST-1 [55].

Given the relatively small reactor volume, low flow rate and efficient mixing, it is likely that the residence time follows the theoretical exponential profile for a CSTR. A key precursor for the synthesis of Zn$_2$(ZnTCPP) is dimethylamine (DMA), a hydrolysis product of DMF, [56,57] which is present in increasing amount throughout the reaction time of a batch reactor. DMA acts as a base and can deprotonate H$_6$TCPP carboxylate group; the initial lag time observed may be due to the initial low DMA concentration. The continuous removal of DMA and addition of fresh DMF throughout the reaction will also inhibit the deprotonation of the H$_6$TCPP precursor to H$_2$TCPP^{4-}, and thereby slow the reaction kinetics relative to the batch process, resulting in a low yield. In principle this could be mitigated by increasing the residence time, or including DMA within a feedstock solution, however DMA is a gas at room temperature and therefore has difficulties associated with feedstock introduction. This insight lead us to investigate the addition of another base to the reaction which we anticipated would enable us to have greater control over the reaction kinetics.

2.2. Addition of triethylamine to the synthesis conditions

Triethylamine (TEA) is commonly used as a base to accelerate MOF crystallisation kinetics through the deprotonation of carboxylate groups enabling co-ordination to metal ions. Inspired by Lapkin and co-workers [30] who used TEA to accelerate reaction kinetics to form Cu(BDC) MONs at room temperature, we explored the effect of adding TEA to our process, initially in batch conditions as in Section 2.1.

Four molar equivalents of TEA was added to the H$_6$TCPP solution prior to the addition of the Zn^{2+} solution. 4:1 TEA:H$_6$TCPP stoichiometry was used as H$_6$TCPP has four carboxylate groups, which have a lower pKa than the central pyrrole units and so are anticipated to preferentially deprotonate. Upon adding the zinc solution, dark
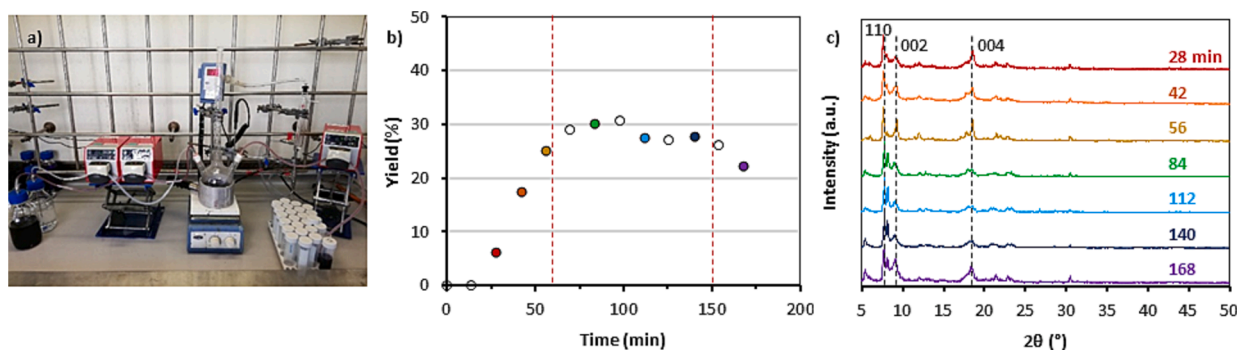
Fig. 2. Operation of the CSTR for MOF production. a) Photograph showing CSTR set-up, pictured without back-end heat exchanger, b) yield of $Zn_2(ZnTCPP)$ isolated from fractions collected throughout the continuous synthesis. Time points refer to the time at start of fraction collection. Filled circles indicate samples analysed using PXRD, for which diffraction patterns are portrayed in c), normalised to the highest intensity of each diffraction pattern and offset for visualisation.

flocculates were observed within seconds which aggregated and dropped from suspension revealing a colourless supernatant (Fig. 3a), indicating very little remaining H_6TCPP in solution. The reaction was allowed to proceed for 1 h before the solids were collected, washed and dried giving a 82 % yield. UV–vis spectroscopy of the resulting material shows four Q-bands (ESI Fig. S10) rather than two, indicative of a lower symmetry,[58] but PXRD of solids indicated the same phase of material was being produced (Fig. 3b). Together, this evidences that the addition of TEA results in a similar overall structure, but the centre of the porphyrin units within the framework are not metalated with zinc, i.e., a framework with the structure $Zn_2(H_2TCPP)$. This is consistent with other low temperature syntheses of porphyrin-based MOFs [59], whilst prolonged reaction times at elevated temperatures are typically required to metalate the centre of the porphyrin units.

After washing through centrifugation, a small amount of solid material was redispersed in EtOH, and an aliquot of this was dried onto a freshly cleaved mica substrate for AFM topographical analysis in order to visualise the particles formed through this rapid crystallisation process. As shown in ESI Fig. S11, this synthesis yielded monolayer $Zn_2(H_2TCPP)$ MONs with lateral dimensions between 50 and 250 nm. Whilst these lateral dimensions are relatively small, this may be beneficial for applications where composite materials are required due to ease of suspending and blending the MONs, and lateral size may not have a significant effect on MON performace in applications such as catalysis and sensing, which make use of sites presented on the 2D surfaces [1].

Forming uniformly monolayer MONs through a bottom-up methodology without the use of surfactants or capping ligands is unusual. H_2TCPP^{4-} can be considered as a highly directional ligand and the square planar coordination motif lends itself well to layer formation. The initial

deprotonation of the ligand precursor by TEA means that highly directional coordination into the 2D layers and rapid reaction kinetics upon mixing in the Zn^{2+} solution promotes the direct crystallisation of $Zn_2(H_2TCPP)$ MONs, i.e., a bottom-up synthesis.

The higher yields achieved with a short reaction time at a low temperature provide a much more attractive route to scale up than our previous high temperature method without TEA, or those previously reported in the literature. Before testing these conditions within the CSTR we also sought to reduce the DMF content as it is relatively expensive and harmful to health and the environment. The ratio of DMF: EtOH used for the batch synthesis with TEA was therefore varied, with v: v ratios of 3:1, 1:1 and 1:3 assessed. Pure EtOH was not investigated as a solvent for synthesis due to the low solubility of the zinc salt. A reaction time of 1 hr was used, and the temperature was controlled at 25 °C to account for differences between ambient room temperature on different days. Solids formed were washed with ethanol, and a small aliquot removed for UV–vis and AFM analyses (Fig. 3c) to assess MON structure and size, then dried and analysed using PXRD (Fig. 3b) to confirm phase. Isolated solids were purple, microcrystalline powders (Fig. 3d,e).

AFM of the materials produced using a 1:1 ratio again showed uniformly monolayer MONs with height ∼ 0.6 nm, with lateral dimensions <300 nm (Fig. 3c). Reducing the DMF content to a 1:1 v:v ratio (corresponding to a 33 % decrease in DMF volume) produced material with a 76 % yield, and PXRD patterns matched the expected phase for $Zn_2(H_2TCPP)$ (Figs. 3b, ESI S12). However, further reduction in the DMF content to a 1:3 ratio resulted in the production of a purple solid with a different, unidentified phase, and therefore no further reduction in DMF content than 1:1 was utilised. The nanosheets suspend similarly well in both ethanol and DMF which may explain why no change in morphology is seen with increasing ethanol content. However, the metal salts are
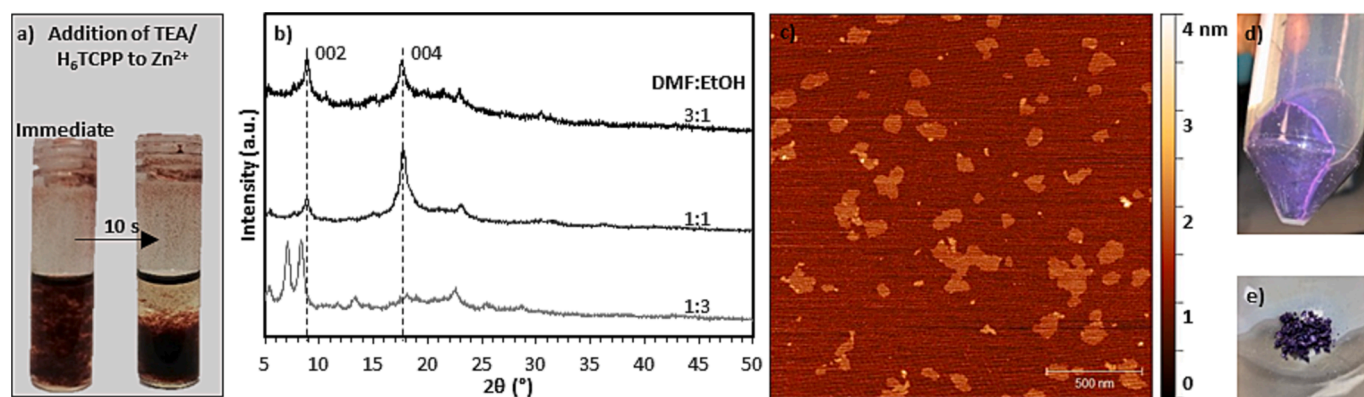

Fig. 3. Characterisation of $Zn_2(H_2TCPP)$ MONs. a) Flocculates and subsequent settling observed upon mixing reagent solutions to form $Zn_2(H_6TCPP)$, b) topographical AFM image of MONs synthesised using 1:1 DMF:EtOH v:v; c) offset PXRD patterns of solids isolated after synthesis using different volume ratios of DMF: EtOH; and photographs of $Zn_2(H_2TCPP)$ d) pellet post-centrifugation and e) dried.

poorly soluble in ethanol so the phase change may be due to a change in effective concentration or more rapid growth kinetics. Further gains could potentially be made by exploring other lower cost or less environmentally damaging solvents or more soluble metal salts, but is beyond the scope of this study.

TCPP nanosheets have been extensively studied in the literature and used in a wide range of applications ranging from water purification and catalysis to sensing and drug delivery [37–48], in part due to their high thermal and chemical stability. The thermal stability of the $Zn_2(H_2TCPP)$ MONs was therefore assessed using thermogravimetric analysis (TGA). The samples were found to be stable up to 300 °C which is typical for this class of MOFs as decarboxylation takes place above this temperature (ESI Fig. S13). An initial mass loss of 13.4 % was observed up to around 200 °C which we ascribe to loss of DMF co-ordinated at the axial positions of the paddle-wheels (expected 13.7 % for $[Zn_2(H_2TCPP).2DMF]$). Chemical stability was also tested through titration of phosphoric acid into an aqueous suspension of the nanosheets, which was monitored by UV–vis spectroscopy. The UV–vis spectra for the nanosheets remained unchanged with a maximum for the Soret band around 424 nm until pH 5.2 below which the Soret band dropped to 416 nm, consistent with dissolution of the nanosheets upon protonation of the carboxylate groups.

## 2.3. Application of optimised conditions to CSTR

The successful room temperature synthesis of MONs using TEA was further scaled-up using a CSTR. The reactor was set-up as described previously, and pump flow rates were varied such that the residence time was 0.5, 1 and 2 h. Solids were collected through centrifugation, and the supernatant was analysed using UV–vis to assess the amount of unreacted H_6TCPP remaining in the reaction mixture. For each residence time, the first collected fraction showed<1 wt% H_6TCPP remaining by UV–vis, indicating a reaction yield >99 %, which was maintained throughout the CSTR operation.

Solids were washed through centrifugation and a 20 μL aliquot removed for UV–vis and AFM analyses, then air-dried, yielding near quantitative isolated solids in all cases (Fig. 4a–c). Due to the rapid reaction kinetics, there was no lag time observed for reaction yield, even for the shortest 30 min residence time. PXRD confirmed the correct phase was produced throughout (ESI Figs S15, 17,19), and UV–vis identified that the porphyrin units were unmetalated throughout each of the synthesis processes (ESI Figs S16, 18, 20). As the reaction proceeded to >99 % completion in each case, increasing the residence time from 0.5 h to 1 and 2 hrs decreased the space–time yield (STY) from 16 kg m^{-3} day^{-1} to 8 and 4 kg m^{-3} day^{-1} respectively.

AFM revealed uniformly monolayer MONs across the different residence times, and throughout each reaction process (ESI Figs. S21–23). It may have been anticipated that upon prolonged reaction time, layers of $Zn_2(H_2TCPP)$ already formed but not yet removed from the reactor could template multilayer MON formation through epitaxial growth, or a nucleation point for multiple nanosheets to grow from, however this was not observed. SEM of an example sample (residence time of 1 hr, final fraction 180–200 mins, ESI Fig. S24) showed discrete lamellar particles of relatively uniform size, <2 μm laterally, consistent with AFM. TGA of the final fraction (180–200 min) collected using residence time of 1 hr showed a similar TGA trace to those observed for the batch material but with an additional mass loss of 3.2 % below 130 °C which was attributed to the presence of water (ESI Fig. S25). This could be due to the ethanol used for bulk synthesis being slightly wetter than for batch synthesis or the difficulties in drying the larger quantities of material.

To investigate process intensification, feedstock concentrations were then increased by four, to [solids] = 0.25 % and the CSTR operated with a residence time of 30 min, in order to increase the STY of MONs produced. UV–vis of centrifuged reaction mixture again showed <1 wt% H_6TCPP remaining, and isolated solids gave a yield >95 % which corresponds to an STY of 64 kg m^{-3} day^{-1}. PXRD patterns and UV–vis spectra corresponded to unmetalated porphyrin units. However, AFM showed that the MONs at this concentration were not monolayer (ESI Fig. S26). MONs were instead observed up to 10 nm thick with lateral dimension <300 nm. Large agglomerates were observed, however this is thought to be a result of the increased concentration and drying process onto the AFM mica substrate as opposed to multiple MONs growing from a central nucleation point, as distinct MONs with edges can be observed. This process likely yields multi-layered (but still ultrathin <10 nm)
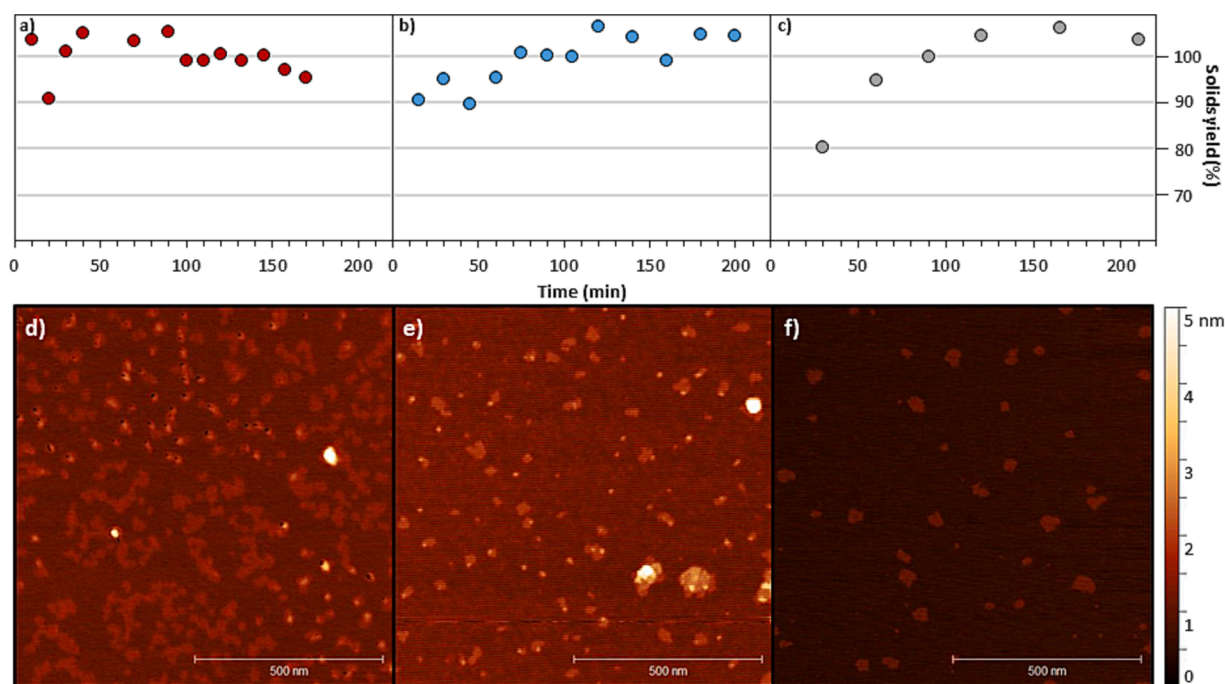
Fig. 4. (a–c) Reaction yields and (d-f) example topographical AFM images from the continuous synthesis of $Zn_2(H_2TCPP)$ MONs at room temperature, using varying residence times of a) 30 m, b) 1 hr and c) 2 h. Time points used are the end of fraction collection (d-f) are each set at the same colour scale, indicated on the right.

MONs due to the increased reagent concentration. Reagent feedstock concentration could be increased further to increase STY, however this would likely increase the thickness of the MONs produced even further.

An alternative method to increased STY is to reduce residence time further. The lowest residence time assessed (0.5 h) produced >95 % yield, with no lag time; it is likely that even lower residence times could be used to produce monolayer MONs, with an associated increase in STY. The reaction kinetics when using TEA also favour the adaptation of the process to alternative rapid-mixing methodologies, such as an annular microreactor, which would enable increased STY as there is no static reactor volume.

2.4. Assessing the economic performance

Three different scenarios were considered: 1) a baseline from literature building on the work by Choi *et al* [51]. and Zhang *et al.*, [52] and 2,3) two scenarios from this work comparing the presence/absence of TEA. The main assumptions for each are shown in Table 2, and all were assessed with the process layout in Fig. 5.

The theoretical pilot plants were designed based on the following processes. Respective solutions were prepared in agitated vessels, which mixed $Zn(NO_3)_2 \cdot 6H_2O$, H_6TCPP and TEA (if used) with appropriate amounts of DMF and EtOH. These solutions were pumped to a jacketed CSTR to yield a suspension of MOF/MON, which was cooled before separation in a filtering centrifuge. The solids were washed in fresh EtOH to remove contaminants, before resuspension in EtOH to form the final product of MOF or MON. Solvents were recovered from the effluent of the centrifuge (including washings) by distillation, with a small fraction (5 %) of both the distilled EtOH and DMF purged for removal of contaminants (for example, solvent degradation products). Recovered solvents were then transferred to respective tanks for intermediate storage (with appropriate make-up of EtOH and DMF), before reintroduction to the mixing vessels for recycled use. All heating and cooling was designed for saturated low-pressure steam and mains water respectively, and all power utilised mains electricity.

Table 2

Scenario assumptions and main results for techno-economic analysis of $Zn_2(XTCPP)$ syntheses (X = H_2 or Zn).

Parameter	Scenarios			Unit
	Literature[†]	This Work (Without TEA)	This Work (With TEA)	
Assumptions				
Reaction temperature	80	120	25	°C
Residence time	180 [a]	50	30	min
Reagent concentration	0.0625	0.0625	0.0625	wt %
Solvent composition (DMF:EtOH)	3:1	3:1	1:1	vol
Product yield	5	28	99	%
Other additive(s)	None	None	TEA	–
Product formed	$Zn_2(ZnTCPP)$ **MOF**	$Zn_2(ZnTCPP)$ **MOF**	$Zn_2(H_6TCPP)$ **MON**	–
Results				
Production Cost	84,700	16,000	5,100	£$_{2020}$/kg
… of which FCC[‡]	1.2	2.3	4.4	%
… of which WCC[‡]	2.3	2.4	2.5	%
… of which FOC[‡]	1.4	5.1	14.4	%
… of which VOC[‡]	95.1	90.2	78.7	%

[†] Choi *et al.* employed a reaction time of 24 h (with a further 9 h for cooling), and other similar syntheses achieved product yields between 53 and 87 %. To remain consistent with this work (without the addition of TEA), a reaction time of 180 min was estimated to be only sufficient to produce MOFs with a product yield of 5 % (based on our investigations of reaction space in batch conditions).

[‡] Acronyms: fixed capital costs (FCC), working capital costs (WCC), fixed operating costs (FOC), variable operating costs (VOC).

In Table 2, it is important to note that monolayer nanosheets were not achieved directly under the literature scenario outlined by Choi *et al* [51] or our synthesis without TEA. Hence, the products in these cases have been designated as $Zn_2(ZnTCPP)$ MOFs, and costly exfoliation and purification steps would be additionally required to afford the corresponding MONs. This exfoliation step has not been considered within this techno-economic model, and instead the respective MOF/MON products are compared as synthesised. Modelling the very long residence times needed to give high yields under the literature conditions implied impractically large reaction vessels. Under batch conditions, a yield of around 5 % was observed after 3 h at a reaction temperature of 80 °C (the literature condition) with no TEA, therefore this shorter reaction time with the correspondingly lower yield was used to provide a benchmark for the techno-economic model.

The main techno-economic results are summarised in Table 2 and Fig. 6. The calculated production costs (PCs) show the syntheses developed in this work offer vast improvements over the baseline scenario. Improvement in PC was largely driven by better conversion of H_6TCPP, which increased from an estimate of just 5 % in the baseline case, to 28 % without TEA and 99 % with TEA (Table 2). This results in a higher efficiency which gives rise to a range of benefits across the entire process: (i) lower variable operating cost (VOC) (e.g., less heating, pumping, reagents, *etc.*); (ii) lower fixed capital costs (FCC) (i.e. smaller processing equipment), and (iii) lower working capital costs (WCC) (i.e., fewer stockpiled chemicals). Fig. 6a shows that even without TEA, the process saw significant reductions in PC of 81 %, but excitingly the negligible additional cost of TEA (and the consequently improved conversion of H_6TCPP) raised savings to 94 %.

Fig. 6b reinforces that the economic viability of these processes is critically reliant on the price of H_6TCPP, where ~59 % of the total PC are attributable to the organic linker for the synthesis with TEA, reduced from ~70 % for the reference synthesis. This is further demonstrated in Fig. 6c, which explored the impact several process parameters (±50 %) on the total PC for the synthesis with TEA (although the other scenarios had largely analogous results). A strong positive correlation existed between the price of H_6TCPP and the total PC: a reduction in the price of H_6TCPP by 30 % would realise significant savings of up to 18 %, for example. Although a techno-economic analysis of the linker synthesis is beyond the scope of this study, the high cost (~£45 g^{-1}) of H_6TCPP means the linker is likely to dominate costs of the manufacture of $Zn_2(H_2TCPP)$ nanosheets, at least on a pilot scale.

The next most important area for improvement is centred around reducing the quantity of solvent used during production, which accounts for ~18 % of PC (Fig. 6b). If the same 30 % improvement could be achieved in solvent purge rate or reaction concentration, the trend in Fig. 6c implies this would realise savings of 5 % each. This is understandable as the extreme dilution of all three syntheses (0.0625 wt% solids) means any reduction in solvent due to (i) increased concentration of the reagents, and/or (ii) better recycling of solvents will have a substantial impact toward reducing PC (for a given production rate). A 30 % variation in unit price for DMF and EtOH saw more modest savings of 4 % and 2 % respectively, with this impact likely driven down by high solvent recycling (95 %, from an assumed purge of 5 %). Lastly, Fig. 6c showed the comparative insensitivity of the process to variation in the cost of capital (WACC), reinforcing that capital requirements are not expected to be prohibitive (at least at pilot scale).

In summary, we have shown that adoption of our developed manufacture process improves techno-economic performance drastically, the main contributor being up to 94 % decrease in PC. This results in a break-even price of £5.10 g^{-1} MON, based on the price for operation of pilot plant producing 400 kg yr^{-1}, for 10 years. This is very favourable compared to those of other components within the chosen high value OPV application (e.g. £72 g^{-1} for P3HT and £240 g^{-1} for PCBM) [60] discussed in Section 2.7. Linker costs are likely to dominate the economics of the synthesis of some other MONs, for example those based on the popular Zr_6BTB systems (where BTB is 1,3,5-benzenetribenzoate)
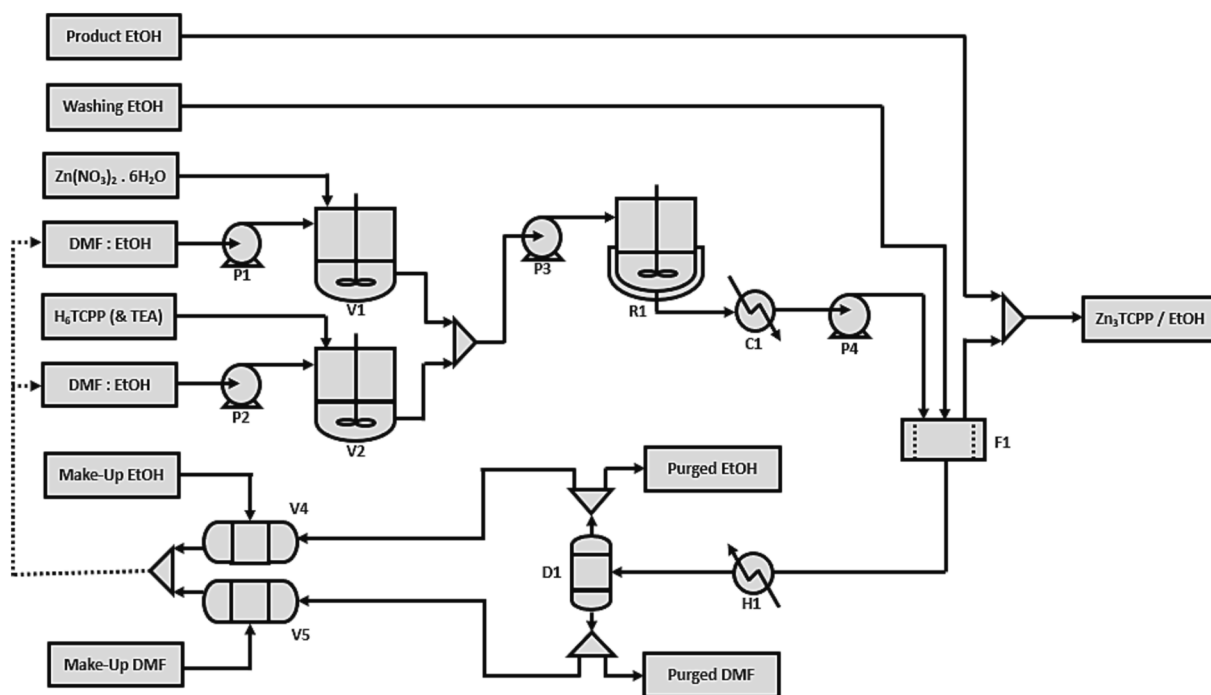
Fig. 5. Process flow diagram considered for the scaled-up synthesis of $Zn_2(ZnTCPP)$ MOF and $Zn_2(H_2TCPP)$ MON.
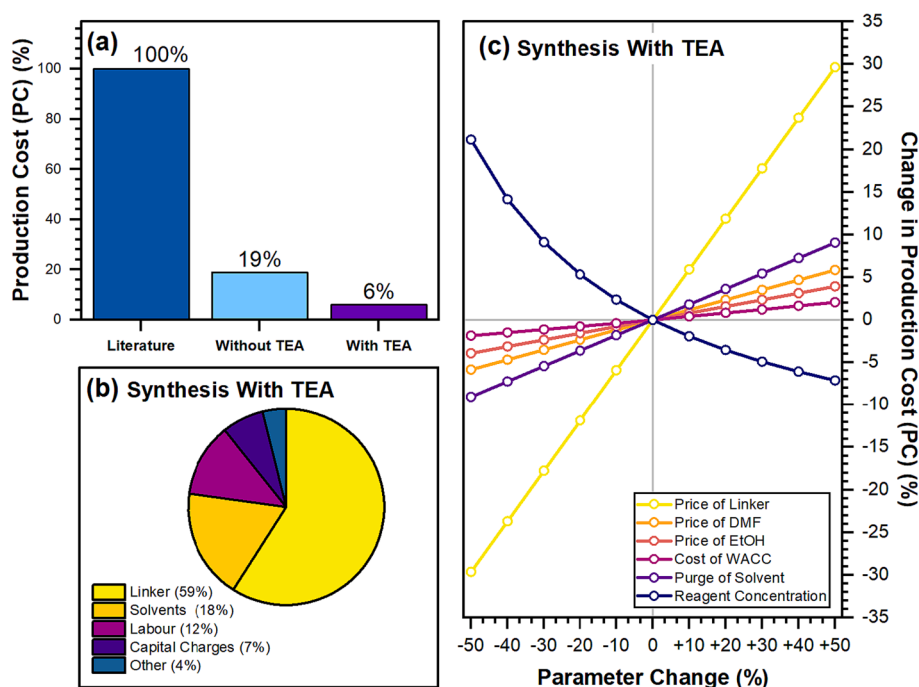

Fig. 6. Techno-economic analyses of $Zn_2(H_2TCPP)$ synthesis scenarios. a) Relative production costs (PC), b) breakdown of costs for the synthesis using TEA, c) sensitivity analysis of PC for the synthesis using TEA.

[16,61]. For other MONs, such as MOF-2 [62] or MIL-53 [63] derived nanosheets, which use terephthalic acid (used to make polyethylene terephthalate (PET) drinks bottles, ~£0.001 g^{-1}), other factors are likely to begin to dominate. In these cases the break-even price will be substantially lower, opening up MON use in lower value applications. The further complete elimination of DMF in our process would be highly desirable not only due to cost reduction but also the safety and practical limitations of working with this solvent at scale. Aqueous or solvent-free methods of MON syntheses [64,65] are highly attractive candidates for scale up. Other insights gained from the scale-up of MOFs are also highly applicable to the formation of nanosheets, for example replacing nitrate salts with safer and lower cost salts could provide further cost savings. Although metal chloride salts are generally cheaper, HCl by-product is destructive for many metal–organic materials, so oxide or hydroxide salts may be preferred, [22,23] where the by-product is water. Promisingly, all of the processes considered here have plenty of scope to be further optimised and intensified, meaning there is likely scope to improve the competitiveness of these MONs.

2.5. Application of process to other MONs

Whilst the cost of manufacture is an important metric for economic viability, the instilled value of materials can be considered as a function of their properties and applications. Manufacturing methods which are easily generalizable and/or adaptable to produce materials with tailored properties are therefore significant. In order to explore the generalisability of our approach we used our CSTR method to synthesise nanosheets of the isostructural copper-based framework, $Cu_2(H_2TCPP)$. This material is also well known (normally as $Cu_2(CuTCPP)$) and has been synthesised using a variety of similar methods to $Zn_2(H_2TCPP)$: at elevated temperature followed by exfoliation to yield MONs, at liquid–air interfaces or using surfactant additives to prevent epitaxial growth [9,66]. These MONs have been exploited in applications including electrochemical devices [67], sensors [66] and gas sieves [45].

The CSTR was run using conditions based on [solids] = 0.0625 wt% and a 30 min residence time in an identical manner to the $Zn_2(H_2TCPP)$ process, using equimolar $Cu(NO_3)_2 \cdot 3H_2O$ instead of $Zn(NO_3)_2 \cdot 6H_2O$, which produced a purple crystalline solid. UV–vis of the reaction mixture supernatant indicated <1 % unreacted H_6TCPP, and solids were collected with an apparent yield over 100 % (ESI Fig. S27). PXRD showed solids were the correct phase (ESI Fig. S28) and UV–vis of MON suspension indicated the porphyrin centres were unmetalated (ESI Fig. S29). The $Cu_2(H_2TCPP)$ MONs observed by AFM were <10 nm in height (ESI Fig. S30) and presented as agglomerates of nanosheets with lateral dimensions < 300 nm. The apparent yield over 100 % indicates that there may be residual solvent held within the pores of the framework, which is possible due to the multilayer structure of these MONs [51] (and not possible for previous monolayer $Zn_2(H_2TCPP)$. The agglomerates observed in AFM are likely a result of MON concentration in the aliquot used for analysis, and the subsequent drying process on the AFM substrate. Multilayer MONs may be due to a combination of factors. Cu^{2+} is a softer ion than Zn^{2+}, and so the reaction kinetics between Cu^{2+} and the deprotonated CO_2^- groups may be slower than for Zn^{2+}/CO_2^-, and so the in-plane reaction is not as heavily favoured, resulting in some epitaxial growth. [68] We expect this approach could also be adapted to synthesise similar MONs with other metals (for e.g. Co, [69] Ni, [70] Al, [37] lanthanides [39] and many others [51]) bound to the porphyrin carboxylate groups.

2.6. Post-synthetic metalation of porphyrin units

The unmetalated porphyrin centres within $Zn_2(H_2TCPP)$ MONs hold an opportunity to introduce a selection of different metal ions through a post-synthetic modification strategy, which offers an element of tunability to the chemical properties of the MONs. Porphyrin-based MONs with different metal centres have been used for a range of catalytic and sensing applications. [1].

$Zn_2(H_2TCPP)$ MONs were dispersed in DMF (2 mg mL^{-1}). Metal (M) salts of Zn, Cu, Ni, Co, Mn, and Cd (see Section 2.2.4. for salts used) were dissolved in DMF. Metal solution was added to MON suspension in a 2:1 stoichiometric ratio of $M:H_2TCPP$, then the mixture was heated under reflux for 2 h, conditions which have been previously demonstrated to quantitatively metalate the porphyrin centres, [71,72] then cooled. From UV–vis spectroscopy, the red shift in soret band (424 to 438 nm) and presence of two Q-bands evidenced the porphyrin units were metalated (Fig. 7a). Small shoulders in Q-bands indicated there may be a very small fraction of unmetalated porphyrin units still present within the MONs. PXRD of the samples indicate phases consistent with the ingoing material (Fig. 7b), each metalated material showed a very similar FTIR spectra (ESI Fig. S31), and ICP-OES of digested samples revealed the Zn:M ratio in the samples (theoretical 2:1) to be 2:1.66, 2:1.35, 2:1.39, 2:2.18 and 2:1.86 for Zn:Cu, Ni, Co, Mn, Cd respectively (Zn-metalated MONs could not be analysed this way). Together, this characterisation shows metalation of the central porphyrin units, yielding MONs with structure $Zn_2(MTCPP)$. The overrepresentation of the inserted metal could be due to metalation of the peripheral carboxylate groups, and/or slight metal exchange with zinc in the paddlewheel units. As an example, AFM of $Zn_2(CoTCPP)$ MONs confirmed they remained monolayer (Figs. 7c, ESI S32).

2.7. Application in organic photovoltaic cells

Solar energy has a vital role to play as our society transitions away from fossil fuels and in creating a more connected world by powering the Internet of Things (IOT). Organic photovoltaic (OPV) cells offer many potential advantages over current silicon-based technologies, such as low-cost production, large area manufacturing and the ability to create flexible, stretchable and semi-transparent devices for use in wearable electronics and powering the IOT [73].We previously demonstrated that the incorporation of $Zn_2(ZnTCPP)$ MONs within the active layer of an organic solar cell resulted in almost doubling of the power conversion efficiency [49]. This was attributed to i) increased fraction of absorbance of the incident solar spectrum resulting from the absorbance contribution of the porphyrin units π-π* Soret band (400–490 nm), and ii) a templating effect of the MONs which increased the fraction of crystalline P3HT domains, which reduced the average grain size and so aided the charge carrier transport. We recently showed that MONs can be used to enhance a wide range of other OPV devices, setting a new record for this extensively studied class of devices [50]. The $Zn_2(ZnTCPP)$ MONs used in these studies were formed using parallel batch MOF syntheses on a 20 mg scale and subsequent exfoliation through sonication producing predominantly monolayer nanosheets with average lateral dimensions of 200 nm. Here, we investigate the performance of the $Zn_2(H_2TCPP)$ MONs synthesised directly from our scalable CSTR method to assess their potential within this high-value
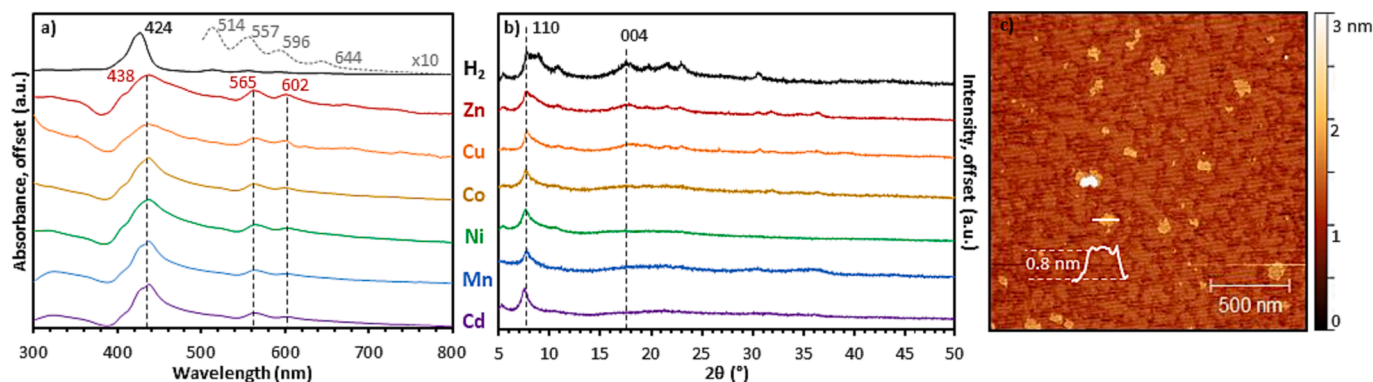
Fig. 7. Post-synthetic metalation of $Zn_2(H_2TCPP$ to form $Zn_2(MTCPP)$ MONs. a) UV–vis spectra and b) PXRD patterns of $Zn_2(H_2TCPP)$ and $Zn_2(MTCPP)$ MONs. H_2 and M refer to what is at the centre of the porphyrin units, e.g. Cu = $Zn_2(CuTCPP)$ MONs. c) AFM topographical image of $Zn_2(CoTCPP)$ MONs.

application (Fig. 8a).

The optical properties of the unmetalated $Zn_2(H_2TCPP)$ were first investigated to determine their suitability for use in OPV devices. There is a blue shift in the major soret absorbance band ($\lambda = 424$ nm, see Fig. 7b) of the unmetalated porphyrin units in the MONs compared to the metalated porphyrin units ($\lambda = 438$ nm). This would result in a small change to the optical band gap, however this was not expected to significantly affect the relative position of the energy levels of MONs with respect to the P3HT donor and PCBM acceptor [49]. We also predicted that the unmetalated porphyrin MONs would not impact the templation effect due to the monolayer morphology and similar size of the nanosheets used. As such, we expected $Zn_2(H_2TCPP)$ MONs to function in a similar way to $Zn_2(ZnTCPP)$ MONs when blended into the ternary photoactive layer within organic photovoltaic cells (Fig. 8b).

The ternary blends of P3HT:$Zn_2(H_2TCPP)$:PCBM (1:0.5:1 wt%) were suspended in chlorobenzene and incorporated into the devices and evaluated for their current–voltage response according to the protocols outlined in reference [49]. The results (Fig. 8c, Table 3) show the maximum power conversion efficiency (PCE_{max}) increased from 2.67 to 4.78 % compared to reference devices without MONs, representing a 79 % increase. These results match well with our previous data (Table 3) demonstrating that $Zn_2(H_2TCPP)$ nanosheets produced using a scalable manufacturing route can achieve comparable results to those achieved for $Zn_2(ZnTCPP)$ nanosheets formed at high temperatures on mg scales using batch processes.

The performance of these devices is ultimately limited by the band gap of P3HT, however the P3HT:PCBM blend is a well-studied and characterised bulk heterojunction device composition and so provides a useful reference material. It is interesting to note that removal of the zinc ion from the porphyrin centre has little effect on device performance which provides further support for our templating hypothesis [49]. Our previous studies indicate that the improvement to device performance observed upon the introduction of $Zn_2(H_2TCPP)$ MONs blended within the active layer should be applicable across a range of high-performance device compositions [50]. Post-synthetic metallation could still provide an opportunity for further fine tuning the opto-electronic and surface properties of the nanosheets, but is beyond the scope of this study. The ability to synthesiseMONs through a low-cost, low-intensity continuous process, could therefore help enable the formation of commercially viable, low cost, high performance organic solar cell device compositions.

3. Conclusions

Metal-organic framework nanosheets (MONs) are a promising new class of 2D material but their use in a wide variety of applications is currently limited by the inefficient, small-scale methods used to prepare them. We have demonstrated the first example of a scalable continuous

Table 3

Device performance metrics for solar cell devices, measured at 25 °C. J_{SC} = short-circuit current density (-mA cm^{-2}); V_{OC} = open circuit voltage (V); FF = fill factor (%); PCE = power conversion efficiency (%).

MONs	J_{sc}	V_{oc}	FF	PCE[†]	PCE_{max}[‡]
None[#]	7.09 ± 0.15	0.66 ± 0.02	57.44 ± 2.20	2.67 ± 0.01	2.67
$Zn_2(ZnTCPP)$[#]	10.54 ± 0.20	0.70 ± 0.03	63.12 ± 0.15	4.65 ± 0.30	5.20
$Zn_2(H_2TCPP)$	10.06 ± 0.68	0.77 ± 0.03	53.90 ± 8.11	4.16 ± 0.52	4.78

[#] Data previously reported in reference [49].
[†] PCE is reported as the average of all workable pixels tested across all devices used.
[‡] PCE_{max} is reported as the maximum average PCE across pixels tested on an individual device.

flow synthesis using a CSTR to directly synthesise monolayer nanosheets in high yield, analysed the economics of this process and demonstrated the use of nanosheets in a high value application.

The literature batch procedure to synthesise $Zn_2(ZnTCPP)$ was systematically modified to enhance the rate of reaction, reduce its cost and environmental impact and translate it into a CSTR process. This demonstrates the applicability of the enhanced synthetic process towards scalable and sustainable manufacturing. Addition of triethylamine as a base dramatically increased the reaction kinetics allowing direct synthesis of monolayer $Zn_2(H_2TCPP)$ nanosheets in high yields and under mild conditions without the need for surfactants or crystal growth modifiers. We also demonstrated the broader applicability of our approach by showing the CSTR could be used to form a wide range of different MONs, either through direct synthesis or post-synthetic metalation.

A techno-economic analysis of our refined process clearly demonstrates the benefits of utilising a high yielding, low-temperature synthesis, enabled through the use of triethylamine. Further optimisation should allow some cost reductions by further reducing the residence time, increasing the space–time yield, decreasing or eliminating DMF use and increasing the solid content. OPEX costs for $Zn_2(H_2TCPP)$ MONs are dominated by the high price of the H_6TCPP ligand and significant investment in the synthesis of this ligand would be needed to substantially reduce the costs of producing TCPP-based MONs.

H_6TCPP was chosen for this study due to its potential for use in high value solar cell applications where the cost of the material produced is comparable to those of other components within the OPV devices. We show that MONs produced using our scalable CSTR approach can lead to near doubling in the performance of archetypal OPV devices. We therefore anticipate that this work will help overcome the challenges in scaling up MONs towards industrial-scale manufacture, to enable their use in a wide range of real-world applications. Further, the methodology
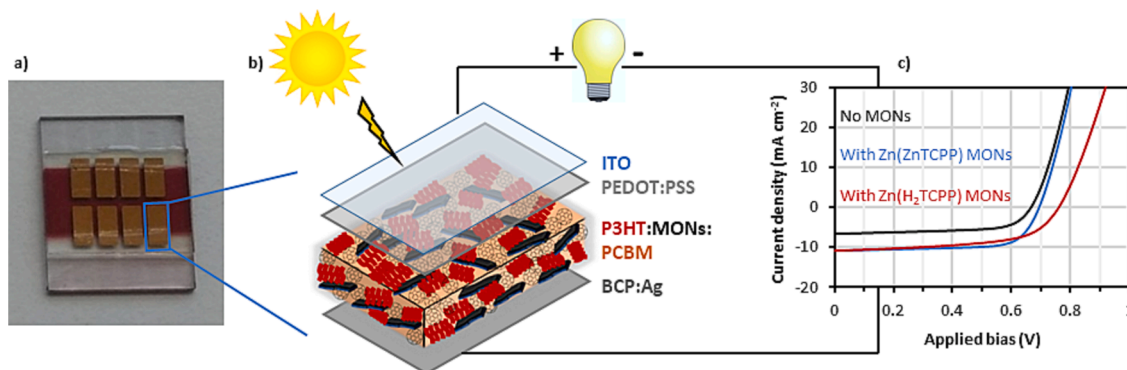
Fig. 8. A) photograph of opv cell; b) schematic diagram portraying opv cell layer compositions and circuitry; c) j-v curves of the best performing devices, with mons (see Fig. 4d) and without MONs present in the photoactive layer (see ESI Fig. 33 for J-V curves of all devices tested).

developed herein, which integrates synthetic and process chemistry, scale-up, manufacture and applications will be of wide interest for developing sustainable and scalable manufacturing for a range of high-value nanomaterials.

4. Experimental

4.1. Materials

All solvents and reagents were purchased from commercial suppliers and used without further purification, other than pyrrole which was distilled prior to use to remove the dimeric impurity which forms over time under storage: pyrrole (Sigma Aldrich, 99.9 %), 4-formylbenzoic acid (Fluorochem, 99 %), propionic acid (Fisher, 99 %), EtOH (Fisher, 99.8 %), DMF (Fisher, 99 %), MeOH (Fisher, 99.8 %), CHCl$_3$ (Fisher, 99.8 %), H$_6$TCPP (Sigma Aldrich, dye content 75 %, and synthesised in-house), Zn(NO$_3$)$_2$·6H$_2$O (Acros organics, 98 %),Cu(NO$_3$)$_2$·3H$_2$O (Sigma Aldrich, 99 %), Co(CH$_3$CO$_2$)$_2$·4H$_2$O (Sigma Aldrich, 98 %), Ni (CH$_3$CO$_2$)$_2$·4H$_2$O (Alfa Aesar, 99 %), Mn(CH$_3$CO$_2$)$_2$·4H$_2$O (Sigma Aldrich, 99 %), and Cd(CH$_3$CO$_2$)$_2$·2H$_2$O (Alfa Aesar, 98 %).

H$_6$TCPP was purchased from Sigma Aldrich (95 %), as well as synthesised in-house. CSTR syntheses of Zn$_2$(H$_2$TCPP) using residence times of 30 mins and 2 h used purchased H$_6$TCPP, all other syntheses used in-house synthesised H$_6$TCPP (ESI Figs S1–S4).

4.2. Methods

H$_6$TCPP synthesis. Tetrakis(4-carboxyphenyl)porphyrin (H$_6$TCPP) was synthesised by adapting a previously reported procedure [74,75]. Pyrrole was freshly distilled prior to use. Pyrrole (1.4 mL, 20 mmol) and 4-formylbenzoic acid (3.02 g, 20 mmol) were added to a 500 mL round bottom flask equipped with a magnetic stirrer bar which was then charged with propionic acid (100 mL). After heating under reflux for 15 h the reaction mixture was cooled to room temperature. The resulting purple precipitate was collected and washed *via* vacuum filtration, with hot water (60 °C), methanol and chloroform. The powder was then dried overnight *in vacuo* (~80 °C) to remove solvent, yielding a dark purple powder of H$_6$TCPP (3.53 g, 89 %). ^{1}H NMR (400 MHz, DMSO-d_6): 8.86 (s, 8H), 8.37 (m, 16H), −2.95 (s, 2H) (ESI Fig. S1 for ^{1}H NMR, and Figs S2–S4 for MS, UV–vis and FTIR spectra).

4.2.1. Batch syntheses of [Zn$_2$(ZnTCPP)] MOF

General set up. H$_6$TCPP (4.5 mg, 0.005 mmol) was dissolved in 4 mL DMF:EtOH mixture (3:1 v:v) and added to a solution of zinc nitrate hexahydrate (4 mg, 0.015 mmol) in 12 mL DMF:EtOH mixture (9:3 v:v) in a glass reaction vial, with a 12 mm Teflon magnetic stirrer bar. The equates to a [solids] = 0.0625 wt%. The reaction mixture was sealed with a Teflon-lined cap and placed in a steel case on a stirrer hot-plate set to the required reaction temperature, under stirring. After the desired time had elapsed, the vial was removed and cooled to room temperature. The contents were transferred to a polyvinylpyrrolidone (PVP) centrifuge tube and solids washed through centrifugation with DMF (3 × 3 mL) and EtOH (3 × 3 mL), then air dried at room temperature, yielding Zn$_2$(ZnTCPP) as a dark purple microcrystalline powder. Yields are based on the anticipated repeat formula unit [Zn$_2$(ZnTCPP) (DMF)$_2$(H$_2$O)]$_n$, where there are DMF molecules coordinated to the axial Zn within the paddlewheel unit, and a water molecule coordinated to the Zn within the porphyrin unit (if present).[49] This is termed, more simply, as Zn$_2$(ZnTCPP) throughout.

Kinetic studies. Three parallel sets of six syntheses were performed at 80, 100 and 120 °C. Reaction mixtures were removed from heat, rapidly cooled to room temperature in ice/water to halt the reaction and then centrifuged to collect solids at time points of 1, 2, 3, 4, 8 and 16 h.

Concentration study. Reaction were set-up according to the general method, but with concentrations increased by 4, 8, 12 and 16 times (equivalent to 0.25, 0.5, 0.75 and 1 wt% solids).

Scaled-up batch. Conditions were selected based on the above experiments. [Solids] = 1 wt% was used and the volume scaled by 12.5 times, to give a total 200 mL solvent volume. To enable the large-volume reaction, the reaction was performed in a 500 mL round-bottom flask under a reflux condenser to minimise solvent loss. N.B. The reaction was open to atmospheric pressure, unlike the small-scale reactions in sealed reaction vials. The reactor was loaded with Zn(NO$_3$)$_2$·6H$_2$O (909.3 mg, 3.057 mmol) in DMF:EtOH (100 mL, 3:1 v:v) and preheated to 110 °C. H$_6$TCPP (808.7 mg, 1.023 mmol) was dissolved in DMF:EtOH (100 mL, 3:1 v:v) and added to the reactor and heated to reflux, 109 °C (boiling point depression caused by the dissolution of reagents in the reaction mixture). The reaction was left for 3 h, then cooled quickly in an ice bath and the contents collected and washed three times with DMF and EtOH through centrifugation (12,000 rpm) and air-dried, yielding Zn$_2$(ZnTCPP) MOF (858.0 mg, 0.749 mmol, 73.5 % yield).

4.2.2. Batch syntheses of [Zn$_2$(H$_2$TCPP)] MONs

Addition of triethylamine (TEA). The synthesis was set up as per the general set up, except TEA (2.1 mg, 2.9 μL, 0.02 mmol) was added to the H$_6$TCPP solution (4:1 stoichiometry of TEA:H$_6$TCPP). Reaction mixture was analysed after 1 hr at 25 °C.

Solvent mixtures. Syntheses were set-up as above, except the starting solutions were made up using 3:1, 1:1 and 1:3 v:v mixtures of DMF:EtOH. Reactions were analysed after 1 h at 25 °C.

Chemical stability test. Aqueous solutions of phosphoric acid (1 mL, various concentrations) were added to a suspension of Zn$_2$(H$_2$TCPP) MONs in EtOH (1 mg mL^{-1}). The shift in absorbance maxima of the Soret band of the TCPP unit was monitored using UV–vis spectroscopy.

4.2.3. Continuous stirred tank reactor set up

Process set-up. The experimental layout of the system was split into three sections: feed (1), reactor (2) and collection (3). (1) The feed section comprised of two feedstock solutions of Zn(NO$_3$)$_2$·6H$_2$O and H$_6$TCPP contained in glass media screwcap bottles at room temperature. Calibrated peristaltic pumps (Watson Marlow, 120S) was used in combination with silicone tubing (d$_i$ = 3 mm) and PTFE tape (for enhanced sealing connections) to feed the reactor, through stainless steel compression fittings (d$_0$ = 1/8 in) secured in bored rubber bungs. (2) The reactor was pre-loaded with an appropriate amount of H$_6$TCPP solution, with a secondary solution of Zn(NO$_3$)$_2$·6H$_2$O prepared to add upon reaction initiation (t = 0), calculated based on the intended residence time of the reactor, in combination with set feed rate of the pumps. The feed tubes drip-fed the reactor from slightly above the solvent line. The reactor was operated under a reflux condenser to minimise solvent loss, which was connected to a bubbler unit filled with mineral oil, to prevent moisture ingress. The reactor temperature was maintained by a thermocouple placed into a surrounding heat jacket. (3) PTFE tubing was used to remove the reaction mixture from the reactor, which was passed through a counter-current double-pipe water-fed heat exchanger, constructed from stainless steel compression fittings with an internal tube for the hot process stream (d$_0$ = 3/8 in) to protect the back-end pump from the high temperature of reaction mixture. Testing showed this exchanger cooled hot reaction mixture from 120 °C to 19 °C. A third calibrated peristaltic pump was used to pump the reaction mixture for collection into new, disposable PVP centrifuge tubes. Samples were collected for 14 min periods then washed three times with EtOH through centrifugation at 12,000 rpm.

High temperature, no additives. Feedstock solutions of Zn (NO$_3$)$_2$·6H$_2$O (281 mg, 0.94 mmol) in 500 mL of 3:1 v:v DMF:EtOH, and H$_6$TCPP (250 mg, 0.32 mmol) in 500 mL of 3:1 v:v DMF:EtOH were prepared. The reactor was loaded with H$_6$TCPP (75 mg, 0.09 mmol) dissolved in 280 mL 3:1 v:v DMF:EtOH, and a solution of Zn (NO$_3$)$_2$·6H$_2$O (84 mg, 0.28 mmol) in 20 mL 3:1 v:v DMF:EtOH was prepared to be added at t = 0. [Solids] was 0.06 %. The reactor was heated to 112 °C (reflux) and the pumps started at t = 0. Residence time was 50 min.

25 °C, with TEA. Feedstock solutions and the reactor pre-loading were calculated based on [solids] = 0.0625 wt%, as for the initial high temperature set-up. Feedstock solutions of $Zn(NO_3)_2 \cdot 6H_2O$ (225 mg, 0.76 mmol) in 400 mL 1:1 v:v DMF:EtOH, and H_6TCPP (200 mg, 0.25 mmol) and TEA (145 uL, 105 mg, 1 mmol) in 400 mL of 1:1 v:v DMF:EtOH were prepared. The reactor was loaded with H_6TCPP (30 mg, 0.04 mmol) and TEA (21.75 μL, 16 mg, 0.16 mmol) in 100 mL of 1:1 v:v DMF:EtOH, and a solution of $Zn(NO_3)_2 \cdot 6H_2O$ (33.75 mg, 0.12 mmol)) in 20 mL of 1:1 v:v DMF:EtOH was prepared to be injected at t = 0. The reactor loadings concentrations differ so that there was only a relatively small volume to be injected, but the resulting mixture is the same [solids] as the combined feed solutions.

Varying residence times. Residence times were varied by adjusting the inlet/outlet flow rates, controlled by the peristaltic pumps. Calibration showed each pump had a flowrate of 1 mL min^{-1} for every 2 rpm (within the low range tested). The back-end pump was therefore operated at twice the rpm of the two front-end pumps. The reactor volume was kept constant at 120 mL. 1 hr residence time was achieved operating the front-end pump at 2 rpm (1 mL min^{-1}), and the back-end at 4 rpm (2 mL min^{-1}). Residence times of 30 mins and 2 hrs were achieved by halving and doubling the flowrates, respectively.

Process intensification. CSTR set-up was as described above for a residence time of 30 mins, other than the concentration of all solutions were increased by a factor of four, resulting in [solids] = 0.25 wt%.

Copper analogue. CSTR set-up was as described for a residence time of 30 mins, [solids] = 0.0625 wt%, other than equimolar metal solutions were made using the suitable mass of $Cu(NO_3)_2 \cdot 3H_2O$ The feedstock solution was made using $Cu(NO_3)_2 \cdot 3H_2O$ (183 mg, 0.75 mmol) in 400 mL 1:1 v:v DMF:EtOH, and the reactor injection solution using $Cu(NO_3)_2 \cdot 3H_2O$ (27 mg, 0.12 mmol) in 20 mL of 1:1 v:v DMF:EtOH.

4.2.4. Post-synthetic metalation

$Zn_2(H_2TCPP)$ MONs were dispersed in DMF (2 mg mL^{-1}, ~2 mol/dm^{-3}(−|−)), with the aid of low power sonication to separate agglomerates. Metal salt solutions were prepared in 5 mL DMF using the metal salts $Zn(NO_3)_2 \cdot 6H_2O$ (5.6 mg), $Cu(NO_3)_2 \cdot 3H_2O$ (4.5 mg), Co$(CH_3CO_2)_2 \cdot 4H_2O$ (4.7 mg), Ni$(CH_3CO_2)_2 \cdot 4H_2O$ (4.7 mg), Mn$(CH_3CO_2)_2 \cdot 4H_2O$ (4.7 mg) and Cd$(CH_3CO_2)_2 \cdot 2H_2O$ (5.1 mg), using masses of metal salt that equate to 0.02 mmol of respective metals.

MON suspension (5 mL, 10 mg of MON, 0.01 mmol MON) was added to metal salt solution (5 mL, 0.02 mmol), in a 50 mL round-bottom flask, which was then refluxed (153 °C) for 2 h. The suspension was cooled to room temperature, MONs washed through centrifugation with DMF (x1) then EtOH (x2) and air-dried at 30 °C, and a small amount redispersed for UV–vis spectroscopy to assess metalation. Solids were analysed using PXRD and FTIR and then used for ICP-OES.

4.3. Characterisation

Powder X-ray Diffraction (PXRD) data were recorded using a Bruker D8 Advance powder X-ray diffractometer equipped with a Lynxeye detector, using Cu k$_\alpha$ radiation (λ = 1.5406 Å) operating in flat-plate mode, using a fixed goniometer stage and rotating sample holder. Samples were sprinkled onto a low-background silicon plate.

Fourier Transform Infrared Spectroscopy (FTIR). Spectra were recorded with a PerkinElmer Spectrum One spectrometer equipped with a diamond ATR accessory. Data were collected from 500 to 4000 cm^{-1} using a resolution of 1 cm^{-1} and 8 scans in air, against a background collection of air.

Thermal Gravimetric Analysis (TGA) was performed on a Perkin-Elmer Pyris TGA from 30 to 700 °C at 10 °C min^{-1}, under a 20 mL min^{-1} nitrogen flow.

Scanning electron microscopy (SEM) samples were prepared on a carbon sticky tab loaded on an aluminium sample stub and coated with approximately 20 nm gold using an Edwards S150B sputter coater. SEM micrographs were collected using a TESCA VEGA3 LMU SEM instrument operating in secondary electron mode.

UV–vis spectroscopy was performed using a Cary 50 UV–vis spectrophotometer with samples inside either a non-absorbing quartz or polystyrene cuvette (for samples in DMF and EtOH, respectively), both path length 10 mm. Samples were scanned at 600 nm s^{-1} using a resolution of 1 nm, against a background of fresh solvent.

^{1}H NMR spectroscopy was performed at room temperature using a Bruker Avance IIIHD 400 MHz spectrometer. ^{1}H chemical shifts are reported in parts per million on the δ scale and referenced to the residual proton resonance of the solvent.

Atomic Force Microscopy (AFM) was performed with a Bruker Multimode 5 AFM operating in soft-tapping mode using Bruker OTESPA-R3 cantilevers (nominal resonance frequency = 290 kHz,). Samples were prepared by drop-casting 10 μL MON suspension onto freshly cleaved mica held on a magnetic sample holder, which was pre-heated to just below the boiling point of the solvent to minimise potential agglomeration upon prolonged drying time. Images were processed using standard techniques within Gwyddion image processing software.

Inductively coupled plasma optical emission spectroscopy (ICP-OES). Samples (~7 mg MON) were digested using 1:0.3 (v:v) nitric acid: perchloric acid and diluted to a suitable concentration. Metal contents were quantified using a Spectro Green ICP-OES spectrometer using argon as the carrier gas and a fluid flow rate of 2 mL min^{-1}.

4.4. Techno-economic assessment

A techno-economic analysis was performed to compare the syntheses of $Zn_2(ZnTCPP)$ MOFs and $Zn_2(H_2TCPP)$ MONs at a pilot-scale (400 kg y^{-1} of MOF/MON). This was performed using a traditional costing procedure as outlined below, full details of which are given in the ESI (Tables S1–S4). Process equipment was sized with heuristics and costed from correlations. [76] These were updated by the respective CEPCI values for 1987 and 2020 (324 and 596), and an assumed exchange rate (~0.79 £$_{2020}$/$$_{2020}$). Capital (CAPEX) and operating (OPEX) expenditures were estimated using a conventional factor method. [77] CAPEX was annualised over the project lifetime with a capital recovery factor (CRF) (Eqn. (1)), assuming a weight average cost of capital (WACC, i = 15 %) and project lifetime (t = 10 y) reflective of the high risk of such a project. Hence, the calculated production cost (PC$_n$, for n = MOF or MON) includes both CAPEX and OPEX components (Eqn. (2)).

$$CRF = \frac{i(1+i)^t}{(1+i)^t - 1} \tag{1}$$

$$PC_n = \frac{CRF(CAPEX_n) + OPEX_n}{\dot{m}_n} \tag{2}$$

Presently, H_6TCPP is sold in gram-quantities at significant cost (~ £45,000/kg), however bulk purchasing is known to substantially reduce unit prices of speciality chemicals. The method by Hart & Sommerfield was used to estimate the bulk price (P_B) of H_6TCPP in bulk quantities (Q_B) based on prices (P_1) and order quantities (Q_1) currently available at laboratory-scale (Eqn. (3)) [78]. The cost exponent (k) was assumed at −0.34 to afford a bulk price for H_6TCPP of £3,700/kg, which was within the range for similarly functionalised porphyrins in the market (~ £2,100 to 6,700/kg,) [79]. Prices for all other chemicals were estimated from existing data at bulk scale, and all scenarios used the same pricing to remain consistent.

$$P_B = P_1 \left(\frac{Q_1}{Q_B}\right)^k \tag{3}$$

4.5. OPV device preparation and testing

Devices were prepared in accordance with our previous study [49]. In brief, pre-patterned ITO glass substrates were sequentially cleaned with hellmanex, boiling water, sonication and isopropyl alcohol, then

dried with a nitrogen gun and cleaned with a UV-ozone cleaner. A PEDOT:PSS solution (Al4083, Ossila) was spin-coated (6000 rpm) onto the substrate to give a film of approximate 25 nm thickness and then annealed (120 °C). The P3HT (Sigma Aldrich), $Zn_2(H_2TCPP)$ MONs and PCBM (99 % purity, Ossila) mixture (1:0.5:1 wt% ratio) was prepared in chlorobenzene then spin-coated (1000 rpm) onto the ITO/PEDOT:PSS substrate with an approximate thickness of 150 nm, then solvent-vapour annealed with chlorobenzene (120 °C). The ITO/PEDOT:PSS/Active layer substrates were then placed under vacuum and covered in layers of thermally evaporated BCP (5 nm) and silver (100 nm) using a shadow mask and the devices were then encapsulated using an epoxy resin (Ossila, E131) with UV cure.

Device performance was determined under ambient conditions by measuring J–V (current density – voltage) curves using a Newport 92251A-1000 solar simulator, with devices illuminated through a 0.0256 cm^2 aperture mask. Before each set of measurements, the intensity was calibrated to 100 mW cm^{-2} using an NREL certified silicon reference cell. The applied bias was swept from 0.0 to + 1.2 V and back again at a scan speed of 0.4 V s^{-1} using a Keithley 237 source measure unit. Eight pixels were assessed from each of five different identically prepared devices. Results are presented as the mean ± standard deviation (not including dead pixels), and the maximum efficiency result presented as the maximum mean performance for a single device. See ESI Fig. S34 for statistical analysis of device performance metrics.

CRediT authorship contribution statement

David J. Ashworth: Conceptualization, Funding acquisition, Methodology, Investigation, Visualization, Writing – original draft, Writing – review & editing. **Justin Driver:** Methodology, Investigation, Visualization, Writing – review & editing. **Kezia Sasitharan:** Investigation, Writing – review & editing. **Ram R.R. Prasad:** Resources, Writing – review & editing. **Joshua Nicks:** Resources, Writing – review & editing. **Benedict J. Smith:** Investigation, Writing – review & editing. **Siddharth V. Patwardhan:** Funding acquisition, Supervision, Writing – review & editing. **Jonathan A. Foster:** Conceptualization, Funding acquisition, Supervision, Project administration, Writing – original draft, Writing – review & editing.

Declaration of Competing Interest

The authors declare that they have no known competing financial interests or personal relationships that could have appeared to influence the work reported in this paper.

Data availability

Data will be made available on request.

Acknowledgements

Appendix A. Supplementary data

Supplementary data to this article can be found online at https://doi.org/10.1016/j.cej.2023.146871.

References

[1] J. Nicks, K. Sasitharan, R.R.R. Prasad, D.J. Ashworth, J.A. Foster, Metal–Organic framework nanosheets: programmable 2D materials for catalysis, sensing, electronics, and separation applications, Adv. Funct. Mater. 31 (42) (2021) 2103723, https://doi.org/10.1002/adfm.202103723.

[2] S. Arun Kumar, et al., Two-dimensional metal organic frameworks for biomedical applications, WIREs Nanomed. Nanobiotechnol. 13 (2) (2021) e1674.

[3] Y. Xue, G. Zhao, R. Yang, F. Chu, J. Chen, L. Wang, X. Huang, 2D metal-organic framework-based materials for electrocatalytic, photocatalytic and thermocatalytic applications, Nanoscale 13 (7) (2021) 3911–3936.

[4] J. Liu, X. Song, T. Zhang, S. Liu, H. Wen, L. Chen, 2D conductive metal-organic frameworks: an emerging platform for electrochemical energy storage, Angew. Chemie Int. Ed. 60 (2021) 5612–5624, https://doi.org/10.1002/anie.202006102.

[5] Y. Zheng, F. Sun, X. Han, J. Xu, X. Bu, Recent progress in 2D metal-organic frameworks for optical applications, Adv. Opt. Mater. 8 (13) (May 2020) 2000110, https://doi.org/10.1002/adom.202000110.

[6] G. Chakraborty, I.-H. Park, R. Medishetty, J.J. Vittal, Two-Dimensional metal-organic framework materials: synthesis, structures, properties and applications, Chem. Rev. 121 (2021) 3751–3891, https://doi.org/10.1021/acs.chemrev.0c01049.

[7] Q. Jiang, C. Zhou, H. Meng, Y. Han, X. Shi, C. Zhan, R. Zhang, Two-dimensional metal-organic framework nanosheets: synthetic methodologies and electrocatalytic applications, J. Mater. Chem. A 8 (31) (2020) 15271–15301.

[8] C. Shi, M.S. Duyar, X. Wang, S. Ye, M. Hu, J. Liu, Design of two-dimensional metal–organic framework nanosheets for emerging applications, FlatChem 29 (2021), 100287, https://doi.org/10.1016/j.flatc.2021.100287.

[9] D.J. Ashworth, J.A. Foster, Metal-organic framework nanosheets (MONs): a new dimension in materials chemistry, J. Mater. Chem. A 6 (34) (2018) 16292–16307, https://doi.org/10.1039/c8ta03159b.

[10] P.-Z. Li, Y. Maeda, Q. Xu, Top-down fabrication of crystalline metal–organic framework nanosheets, Chem. Commun. 47 (29) (2011) 8436–8438, https://doi.org/10.1039/c1cc12510a.

[11] Q. Qiu, H. Chen, Z. You, Y. Feng, X. Wang, Y. Wang, Y. Ying, Shear Exfoliated metal-organic framework nanosheet enabled flexible sensor for real-time monitoring of superoxide anion shear exfoliated metal-organic framework nanosheet enabled flexible sensor for real-time monitoring of superoxide anion, ACS Appl. Mater. Interfaces 12 (5) (2020) 5429–5436.

[12] Y. Peng, et al., Metal-organic framework nanosheets as building blocks for molecular sieving membranes, Science 80-.) 346 (6215) (2014) 1356–1359, https://doi.org/10.1126/science.1260139.

[13] T. Kambe, R. Sakamoto, K. Hoshiko, K. Takada, M. Miyachi, J.-H. Ryu, S. Sasaki, J. Kim, K. Nakazato, M. Takata, H. Nishihara, π-Conjugated nickel bis(dithiolene) complex nanosheet, J. Am. Chem. Soc. 135 (7) (2013) 2462–2465.

[14] G. Xu, K. Otsubo, T. Yamada, S. Sakaida, H. Kitagawa, Superprotonic conductivity in a highly oriented crystalline metal– organic framework nanofilm, J. Am. Chem. Soc. 135 (20) (2013) 7438–7441, https://doi.org/10.1021/ja402727d.

[15] R. Sakamoto, K. Hoshiko, Q. Liu, T. Yagi, T. Nagayama, S. Kusaka, M. Tsuchiya, Y. Kitagawa, W.-Y. Wong, H. Nishihara, A photofunctional bottom-up bis (dipyrrinato)zinc(II) complex nanosheet, Nat. Commun. 6 (1) (2015), https://doi.org/10.1038/ncomms7713.

[16] L. Cao, Z. Lin, F. Peng, W. Wang, R. Huang, C. Wang, J. Yan, J. Liang, Z. Zhang, T. Zhang, L. Long, J. Sun, W. Lin, Self-supporting metal-organic layers as single-site solid catalysts, Angew. Chemie Int. Ed. 55 (16) (2016) 4962–4966.

[17] S.C. Junggeburth, L. Diehl, S. Werner, V. Duppel, W. Sigle, B.V. Lotsch, Ultrathin 2D coordination polymer nanosheets by surfactant-mediated synthesis, J. Am. Chem. Soc. 135 (16) (2013) 6157–6164, https://doi.org/10.1021/ja312567v.

[18] H. Ang, L. Hong, Polycationic polymer-regulated assembling of 2D MOF Nanosheets for high-performance nanofiltration, ACS Appl. Mater. Interfaces 9 (33) (2017) 28079–28088, https://doi.org/10.1021/acsami.7b08383.

[19] B. Wang, J. Shang, C. Guo, J. Zhang, F. Zhu, A. Han, J. Liu, A general method to ultrathin bimetal-MOF nanosheets arrays via in situ transformation of layered double hydroxides arrays, Small 15 (6) (2019), https://doi.org/10.1002/smll.201804761.

[20] L. Zhuang, L. Ge, H. Liu, Z. Jiang, Y.i. Jia, Z. Li, D. Yang, R.K. Hocking, M. Li, L. Zhang, X. Wang, X. Yao, Z. Zhu, A surfactant-free and scalable general strategy for synthesizing ultrathin two-dimensional metal-organic framework nanosheets for the oxygen evolution reaction, Angew. Chemie Int. Ed. 131 (38) (2019) 13699–13706.

[21] R. Pilling, S. R. Coles, M. Knecht, and S. V. Patwardhan, "Realising Nanomaterial Potential Through Multi-Criteria Discovery, Design and Manufacturing," *submitted.*

[22] X.J. Kong, J.R. Li, An overview of metal-organic frameworks for green chemical engineering, Engineering 7 (8) (2021) 1115–1139, https://doi.org/10.1016/j.eng.2021.07.001.

[23] M. Rubio-Martinez, C. Avci-Camur, A.W. Thornton, I. Imaz, D. Maspoch, M.R. Hill, New synthetic routes towards MOF production at scale, Chem. Soc. Rev. 46 (11) (2017) 3453–3480, https://doi.org/10.1039/c7cs00109f.

[24] Q. He, F. Zhan, H. Wang, W. Xu, H. Wang, L. Chen, Recent progress of industrial preparation of metal–organic frameworks: synthesis strategies and outlook, Mater. Today Sustain. 17 (2022), 100104, https://doi.org/10.1016/j.mtsust.2021.100104.

[25] M. Rubio-Martinez, T.D. Hadley, M.P. Batten, K. Constanti-Carey, T. Barton, D. Marley, A. Mönch, K.-S. Lim, M.R. Hill, Scalability of continuous flow production of metal-organic frameworks, ChemSusChem 9 (9) (2016) 938–941.

[26] J. Ren, X. Dyosiba, N.M. Musyoka, H.W. Langmi, M. Mathe, S. Liao, Review on the current practices and efforts towards pilot-scale production of metal-organic

frameworks (MOFs), Coord. Chem. Rev. 352 (2017) 187–219, https://doi.org/10.1016/j.ccr.2017.09.005.

[27] W.L. Teo, W. Zhou, C. Qian, Y. Zhao, Industrializing metal–organic frameworks: Scalable synthetic means and their transformation into functional materials, Mater. Today 47 (August) (2021) 170–186, https://doi.org/10.1016/j.mattod.2021.01.010.

[28] J.E. Chen, Z.-J. Yang, H.U. Koh, J. Shen, Y. Cai, Y. Yamauchi, L.-H. Yeh, V. Tung, K.-W. Wu, Current progress and scalable approach toward the synthesis of 2D metal-organic frameworks, Adv. Mater. Interfaces 9 (13) (2022), https://doi.org/10.1002/admi.202102560.

[29] Y. Wang, L. Li, L. Yan, X. Gu, P. Dai, D. Liu, J.G. Bell, G. Zhao, X. Zhao, K. M. Thomas, Bottom-up fabrication of ultrathin 2D Zr metal-organic framework nanosheets through a facile continuous microdroplet flow reaction, Chem. Mater. 30 (9) (2018) 3048–3059.

[30] N.A. Jose, H.C. Zeng, A.A. Lapkin, Scalable and precise synthesis of two-dimensional metal organic framework nanosheets in a high shear annular microreactor, Chem. Eng. J. 388 (2020), 124133, https://doi.org/10.1016/j.cej.2020.124133.

[31] C. Hu, Reactor design and selection for effective continuous manufacturing of pharmaceuticals, J. Flow Chem. 11 (3) (2021) 243–263, https://doi.org/10.1007/s41981-021-00164-3.

[32] R. Pilling, S.V. Patwardhan, Recent advances in enabling green manufacture of functional nanomaterials: a case study of bioinspired silica, ACS Sustain. Chem. Eng. 10 (37) (2022) 12048–12064, https://doi.org/10.1021/acssuschemeng.2c02204.

[33] C. McKinstry, R.J. Cathcart, E.J. Cussen, A.J. Fletcher, S.V. Patwardhan, J. Sefcik, Scalable continuous solvothermal synthesis of metal organic framework (MOF-5) crystals, Chem. Eng. J. 285 (2016) 718–725, https://doi.org/10.1016/j.cej.2015.10.023.

[34] C. McKinstry, E.J. Cussen, A.J. Fletcher, S.V. Patwardhan, J. Sefcik, Effect of synthesis conditions on formation pathways of metal organic framework (MOF-5) crystals, Cryst. Growth Des. 13 (12) (2013) 5481–5486, https://doi.org/10.1021/cg4014619.

[35] H. L. B. Boström *et al.*, "How reproducible is the synthesis of Zr-porphyrin metal-organic frameworks ? An interlaboratory study," *Adv. Mater.*, vol. accepted.

[36] S. Motoyama, R. Makiura, O. Sakata, H. Kitagawa, Highly crystalline nanofilm by layering of porphyrin metal-organic framework sheets, J. Am. Chem. Soc. 133 (15) (2011) 5640–5643, https://doi.org/10.1021/ja110720f.

[37] Z. Zhou, T. Wang, T. Hu, C. Cheng, S. Yu, H. Li, S. Liu, L. Ma, M. Zhao, R. Liang, C. Tan, Facile synthesis of 2D Al-TCPP MOF nanosheets for efficient sonodynamic cancer therapy, Mater. Chem. Front. 7 (8) (2023) 1684–1693.

[38] B. Yang, H. Yao, J. Yang, C. Chen, J. Shi, Construction of a two-dimensional artificial antioxidase for nanocatalytic rheumatoid arthritis treatment, Nat. Commun. 13 (1) (2022) 1988, https://doi.org/10.1038/s41467-022-29735-1.

[39] Z.W. Jiang, Y.C. Zou, T.T. Zhao, S.J. Zhen, Y.F. Li, C.Z. Huang, Controllable synthesis of porphyrin-based 2D lanthanide metal-organic frameworks with thickness- and metal-node-dependent photocatalytic performance, Angew. Chemie Int. Ed. 621900 (2020) 3300–3306, https://doi.org/10.1002/anie.201913748.

[40] Z. Sun, S. Wu, Y. Peng, M. Wang, M. Jalalah, M.S. Al-Assiri, F.A. Harraz, J. Yang, G. Li, Sensor array for rapid pathogens identification fabricated with peptide-conjugated 2D metal-organic framework nanosheets, Chemical Engineering Journal 405 (2021) 126707.

[41] Q. Qiu, H. Chen, S. Ying, S. Sharif, Z. You, Y. Wang, Y. Ying, Simultaneous fluorometric determination of the DNAs of salmonella enterica, listeria monocytogenes and vibrio parahemolyticus by using an ultrathin metal-organic framework (type Cu-TCPP), Microchim. Acta 186 (2) (2019), https://doi.org/10.1007/s00604-019-3226-y.

[42] Z. Qiu, T. Yang, R. Gao, G. Jie, W. Hou, An electrochemical ratiometric sensor based on 2D MOF nanosheet/Au/polyxanthurenic acid composite for detection of dopamine, Journal of Electroanalytical Chemistry 835 (2019) 123–129.

[43] H. Chen, Q. Qiu, S. Sharif, S. Ying, Y. Wang, Y. Ying, Solution-phase synthesis of platinum nanoparticle-decorated metal-organic framework hybrid nanomaterials as biomimetic nanoenzymes for biosensing applications, ACS Appl. Mater. Interfaces 10 (28) (2018) 24108–24115, https://doi.org/10.1021/acsami.8b04737.

[44] W. Zhao, et al., Wrinkled two-dimensional ultrathin Cu(ii)-porphyrin framework nanosheets hybridized with polypyrrole for flexible all-solid-state supercapacitors, Dalt. Trans. 48 (2019) 6931–9638, https://doi.org/10.1039/c8dt05069d.

[45] Y. Song, Y. Sun, D. Du, M.u. Zhang, Y.i. Liu, L. Liu, T. Ji, G. He, Y.i. Liu, Fabrication of c-oriented ultrathin TCPP-derived 2D MOF membrane for precise molecular sieving, J. Memb. Sci. 634 (2021), 119393, https://doi.org/10.1016/j.memsci.2021.119393.

[46] A. Yao, et al., Integration of P84 and porphyrin–based 2D MOFs (M−TCPP, M = Zn, Cu Co, Ni) for mixed matrix membranes towards enhanced performance in organic solvent nanofiltration, Sep. Purif. Technol. vol. 282, no. PA (2022), 120022, https://doi.org/10.1016/j.seppur.2021.120022.

[47] M. Liu, K.e. Xie, M.D. Nothling, P.A. Gurr, S.S.L. Tan, Q. Fu, P.A. Webley, G. G. Qiao, Ultrathin metal-organic framework nanosheets as a gutter layer for flexible composite gas separation membranes, ACS Nano 12 (11) (2018) 11591–11599.

[48] G. Ding, Y. Wang, G. Zhang, K. Zhou, K. Zeng, Z. Li, Y.e. Zhou, C. Zhang, X. Chen, S.-T. Han, 2D metal-organic framework nanosheets with time-dependent and multilevel memristive switching, Adv. Funct. Mater. 29 (3) (2019), https://doi.org/10.1002/adfm.201806637.

[49] K. Sasitharan, D.G. Bossanyi, N. Vaenas, A.J. Parnell, J. Clark, A. Iraqi, D.G. Lidzey, J.A. Foster, Metal-organic framework nanosheets for enhanced performance of organic photovoltaic cells, J. Mater. Chem. A 8 (12) (2020) 6067–6075.

[50] K. Sasitharan, R.C. Kilbride, E.L.K. Spooner, J. Clark, A. Iraqi, D.G. Lidzey, J. A. Foster, Metal-Organic framework nanosheets as templates to enhance performance in semi-crystalline organic photovoltaic cells, Adv. Sci. 9 (21) (2022), https://doi.org/10.1002/advs.202200366.

[51] E.Y. Choi, C.A. Wray, C. Hu, W. Choe, Highly tunable metal-organic frameworks with open metal centers, CrystEngComm 11 (4) (2009) 553–555, https://doi.org/10.1039/b819707p.

[52] M. Zhao, Y. Wang, Q. Ma, Y. Huang, X. Zhang, J. Ping, Z. Zhang, Q. Lu, Y. Yu, H. Xu, Y. Zhao, H. Zhang, Ultrathin 2D metal-organic framework nanosheets, Adv. Mater. 27 (45) (2015) 7372–7378.

[53] M. Jian, H. Liu, T. Williams, J. Ma, H. Wang, X. Zhang, Temperature-induced oriented growth of large area, few-layer 2D metal-organic framework nanosheets, Chem. Commun. 53 (98) (2017) 13161–13164, https://doi.org/10.1039/c7cc06988j.

[54] P.M. Schoenecker, G.A. Belancik, B.E. Grabicka, K.S. Walton, Kinetics study and crystallization process design for scale-up of UiO-66-NH2 synthesis, AIChE J. 59 (4) (Apr. 2013) 1255–1262, https://doi.org/10.1002/aic.13901.

[55] F. Millange, R. El Osta, M.E. Medina, R.I. Walton, A time-resolved diffraction study of a window of stability in the synthesis of a copper carboxylate metal-organic framework, CrystEngComm 13 (1) (2011) 103–108, https://doi.org/10.1039/c0ce00530d.

[56] Q. Yang, M. Sheng, Y. Huang, Potential safety hazards associated with using N, N-Dimethylformamide in chemical reactions, Org. Process Res. Dev. 24 (9) (2020) 1586–1601, https://doi.org/10.1021/acs.oprd.0c00330.

[57] Y. Wan, M. Alterman, M. Larhed, A. Hallberg, Dimethylformamide as a carbon monoxide source in fast palladium-catalyzed aminocarbonylations of aryl bromides, J. Org. Chem. 67 (17) (2002) 6232–6235, https://doi.org/10.1021/jo025965a.

[58] T. Hashimoto, Y.-K. Choe, H. Nakano, K. Hirao, Theoretical study of the Q and B bands of free-base, magnesium, and zinc porphyrins, and their derivatives, J. Phys. Chem. A 103 (12) (1999) 1894–1904.

[59] M.C. So, S. Jin, H.J. Son, G.P. Wiederrecht, O.K. Farha, J.T. Hupp, Layer-by-layer fabrication of oriented porous thin films based on porphyrin-containing metal-organic frameworks, J. Am. Chem. Soc. 135 (42) (2013) 15698–15701, https://doi.org/10.1021/ja4078705.

[60] "Ossila." [Online]. Available: https://www.ossila.com/. [Accessed: 25-May-2023].

[61] Y. Wang, L. Feng, J. Pang, J. Li, N. Huang, G.S. Day, L. Cheng, H.F. Drake, Y. e. Wang, C. Lollar, J. Qin, Z. Gu, T. Lu, S. Yuan, H.-C. Zhou, Photosensitizer-anchored 2D MOF nanosheets as highly stable and accessible catalysts toward artemisinin production, Adv. Sci. 6 (11) (2019), https://doi.org/10.1002/advs.201802059.

[62] T. Rodenas, I. Luz, G. Prieto, B. Seoane, H. Miro, A. Corma, F. Kapteijn, F.X. Llabrés i Xamena, J. Gascon, Metal-organic framework nanosheets in polymer composite materials for gas separation, Nat. Mater. 14 (1) (2015) 48–55.

[63] A. Pustovarenko, M.G. Goesten, S. Sachdeva, M. Shan, Z. Amghouz, Y. Belmabkhout, A. Dikhtiarenko, T. Rodenas, D. Keskin, I.K. Voets, B. M. Weckhuysen, M. Eddaoudi, L.C.P.M. de Smet, E.J.R. Sudhölter, F. Kapteijn, B. Seoane, J. Gascon, Nanosheets of nonlayered aluminum metal-organic frameworks through a surfactant-assisted method, Adv. Mater. 30 (26) (2018), https://doi.org/10.1002/adma.201707234.

[64] J. Zhang, J. Liu, X. Li, Y. Xu, Solvent-free synthesis of hierarchical Tb3+-doped Yttrium benzene-1,3,5-tricarboxylate metal organic framework nanosheets for fast and highly sensitive fluorescence detection of Fe3+ and Cr2O72− ions, Resour. Chem. Mater. 1 (2) (2022) 146–151, https://doi.org/10.1016/j.recm.2022.06.001.

[65] F. Xu, Y. Zhou, X. Zhai, H. Zhang, H. Liu, E.H. Ang, Y. Lu, Z. Nie, M. Zhou, J. Zhu, Ultrafast universal fabrication of metal-organic complex nanosheets by joule heating engineering, Small Methods 6 (1) (2022), https://doi.org/10.1002/smtd.202101212.

[66] L. Zhao, Y. Zhao, R. Li, D. Wu, X. Xie, H. Ye, Y. Zhang, Q. Xin, Insights into the binding mechanism of 2D copper-tetrakis-(4-carboxyphenyl)-porphyrin metal-organic framework nanosheets with Rhodamine B: spectroscopic and thermodynamics studies, Chemical Physics 534 (2020) 110743.

[67] S. Lei, L.-M. Chang, Z.-G. Gu, J. Zhang, Metal-Porphyrinic framework film as efficient optical limiting layer in electro-optical switchable device, Chem. Commun. 57 (2021) 10166–10169, https://doi.org/10.1039/d1cc04513j.

[68] H. Jiang, Q. Fu, H. Liang, L. Yan, L. Yang, Y. Wang, J. Zhang, X. Zhao, Growth process of two-dimensional metal-organic framework Cu-BDC: a particle attachment crystallization mechanism revealed by microdroplet flow reaction, Cryst. Growth Des. 23 (4) (2023) 2845–2851.

[69] Y. Wang, M. Zhao, J. Ping, B.o. Chen, X. Cao, Y. Huang, C. Tan, Q. Ma, S. Wu, Y. Yu, Q. Lu, J. Chen, W. Zhao, Y. Ying, H. Zhang, Bioinspired design of ultrathin 2D bimetallic metal-organic-framework nanosheets used as biomimetic enzymes, Adv. Mater. 28 (21) (2016) 4149–4155.

[70] A. Yao, et al., Integration of P84 and porphyrin-based 2D MOFs (M-TCPP, M = Zn, Cu Co, Ni) for mixed matrix membranes towards enhanced performance in organic solvent nanofiltration, Sep. Purif. Technol. 282 (2022), 120022.

[71] E.B. Fleischer, A.M. Shachter, Coordination oligomers and a coordination polymer of zinc tetraarylporphyrins, Inorg. Chem. 30 (19) (1991) 3763–3769, https://doi.org/10.1021/ic00019a038.

[72] B.M.J.M. Suijkerbuijk, R.J.M. Klein Gebbink, Merging porphyrins with organometallics: synthesis and applications, Angew. Chemie Int. Ed. 47 (39) (2008) 7396–7421, https://doi.org/10.1002/anie.200703362.

[73] P. Cheng, G. Li, X. Zhan, Y. Yang, Next-generation organic photovoltaics based on non-fullerene acceptors, Nat. Photonics 12 (3) (2018) 131–142, https://doi.org/10.1038/s41566-018-0104-9.

[74] T. Rhauderwiek, S. Waitschat, S. Wuttke, H. Reinsch, T. Bein, N. Stock, Nanoscale synthesis of two porphyrin-based MOFs with gallium and indium, Inorg. Chem. 55 (11) (2016) 5312–5319, https://doi.org/10.1021/acs.inorgchem.6b00221.

[75] F.R. Longo, M.G. Finarelli, J.B. Kim, The synthesis and some physical properties of ms-tetra(pentafluorophenyl)-porphin and ms-tetra(pentachlorophenyl)porphin, J. Heterocycl. Chem. 6 (6) (1969) 927–931, https://doi.org/10.1002/jhet.5570060625.

[76] D.E. Garrett (Ed.), Chemical Engineering Economics, Springer Netherlands, Dordrecht, 1989.

[77] R. K. Sinnott, *Coulson & Richardson ' s Chemical Engineering: Chemical Engineering Design*, 4th ed., vol. 6. Oxford: Elsevier Butterworth-Heinemann, 2005.

[78] P.W. Hart, J.T. Sommerfeld, Cost estimation of specialty chemicals from laboratory-scale prices, Cost Eng. 39 (3) (1997) 31–35.

[79] "Porphyrin-Laboratories." [Online]. Available: https://porphyrin-laboratories.com/eng/bulk/porphien-bulk-quantities.php. [Accessed: 23-Apr-2023].